Investigating the Time Evolution of Plasma Density Structures in the ZaP-HD Flow Z-pinch

Harry Furey-Soper

A thesis
submitted in partial fulfillment of the
requirements for the degree of

Master of Science

University of Washington

2025

Committee:

Uri Shumlak

Bhuvana Srinivasan

Program Authorized to Offer Degree:

Aeronautics and Astronautics

University of Washington

Abstract

Investigating the Time Evolution
of Plasma Density Structures in the
ZaP-HD Flow Z-pinch

Harry Furey-Soper

Chair of the Supervisory Committee:
Uri Shumlak
Aeronautics and Astronautics

The Sheared-Flow-Stabilized Z-pinch is understood to be a promising plasma confinement configuration for applications in fusion energy. The application of a radial velocity shear offers stabilization against the Magneto-Rayleigh-Taylor instability, which causes classical Z-pinch plasmas to collapse at the densities and temperatures required for thermonuclear fusion. This thesis aims to characterize the spatiotemporal evolutions of electron density structures in the ZaP-HD Flow Z-pinch device using a 4-chord laser interferometer. The interferometer is based on a modified Mach-Zehnder configuration, and employs heterodyne and quadrature signal processing techniques. The most significant deviation from the standard Mach-Zehnder is the use of scene and reference beams with unequal path lengths. Data from a benchtop proof-of-concept experiment is provided to demonstrate the functionality of the unequal path configuration. The region of interest for this investigation is the segment of the pinch extending 20-30 centimeters axially downstream of the outlet of the coaxial accelerator in the ZaP-HD device, which is responsible for producing the radial shear. Data from an earlier science campaign is briefly discussed as motivation for the study of density structures in this specific region. Interferometer data is presented and analyzed to obtain characteristic scale lengths of density gradients. Analysis of the interferometer data is supported by data from a fast-framing camera and azimuthal magnetic field probes.

TABLE OF CONTENTS

Page

LIST OF FIGURES

ACKNOWLEDGMENTS

I wish to express my gratitude and appreciation to several individuals who supported me along my journey to produce this work.

Professor Uri Shumlak, the committee chair for this work, has supported me in my exploration of the field of plasma physics since my undergraduate studies. His guidance has pushed me to be a better scientist at every opportunity.

Professor Bhuvana Srinivasan contributed to improving my knowledge of the fundamental physics of wave propagation in a plasma, and guided me towards a better understanding of the tools used in my research.

The camaraderie of Aqil, Jared, Elliot, Zhangsheng, Aria, Bennett, Shane, Jeff, and all of my colleagues in the ZaP-HD laboratory made the good days better and the rough days tolerable.

My parents Spencer and Susan, and my fiancée Faith, have provided immensely valuable support throughout my academic journey thus far. This work would not have been completed without them in my corner.

Chapter 1

INTRODUCTION

1.1 Nuclear Fusion

Individual atomic nuclei are held together by the strong nuclear force, an attractive force which bonds protons and neutrons and acts over a characteristic length scale comparable to the diameter of one nucleon. If two atomic nuclei approach each other at a close enough proximity, the attraction between them due to the strong nuclear force will cause them to fuse into a larger single nucleus. Such an event is known as a nuclear fusion reaction. However, separate atomic nuclei are kept apart from each other by the electrostatic repulsive force between the positively charged protons in the atomic nuclei. The peak magnitude of the nuclear strong force is significantly larger than that of the electrostatic force, however, the electrostatic force acts over much longer distances. This presents the idea of a shell of some radius around an atomic nucleus, such that the attractive nuclear strong force is dominant inside of the shell, and the repulsive electrostatic force is dominant outside of the shell. This shell is known as the Coulomb barrier. Therefore, for a nuclear fusion reaction to occur, two atomic nuclei must approach each other at some relative velocity such that they collide with sufficient kinetic energy to penetrate the Coulomb barrier.

The study of nuclear fusion has a variety of useful applications including astrophysical sciences, radioisotope production, medicine, and space propulsion. The application which almost certainly has the greatest potential societal impact, is the production of clean and renewable energy. For the purposes of this thesis, energy will be the primarily discussed application.

1.1.1 Early History

In the year of 1921, Francis William Aston delivered a lecture to the Chemical Society of London (now known as the Royal Society of Chemistry) summarizing his experimental measurements of the atomic weights of various elements. His research revealed that a helium nucleus consisting of 2 protons and 2 neutrons, ^4He, was lighter in mass than 4 protons, or 4 hydrogen nuclei ^1H [3]. In the decade following this discovery, research was conducted to connect this mass inequality to phenomena observed in the natural world. The hypothesis that hydrogen nuclei could be combined into larger nuclei, through some process releasing a quantity of energy equivalent to the mass lost as described by $E = mc^2$, became the leading explanation for how stars produce energy [4]. This hypothesis was supported by the discovery of the quantum tunneling effect, which enables positively-charged atomic nuclei to fuse at lower collision energies than required to overcome the classically understood Coulombic repulsion forces [5]. The first man-made fusion reaction was observed in 1934 by Mark Oliphant, during a particle accelerator experiment in which two deuterons[1] collided to produce a proton and a triton[2] , with the products having a combined kinetic energy greater than the collision energy of the constituents [6]. Humanity had now proven two critical postulates. The first being that a small fraction of the mass within an atomic nucleus could be destroyed in exchange for a positive net output of kinetic energy, and the second being that such a reaction could be produced artificially in a man-made device. Therefore, it was inevitable for humanity to pursue nuclear fusion as a source of terrestrial energy production.

1.1.2 Fusion Reactions and Energy Output

The deuterium-deuterium fusion reaction observed in Mark Oliphant's particle accelerator experiment produces a triton and a proton with kinetic energies of approximately 1 MeV and 3 MeV, respectively. The reactants, products, and associated energies of many fusion reactions have been determined through empirical investigations. Three of these reactions

[1] A deuteron is a single nucleus of deuterium, which is an isotope of hydrogen containing one neutron.

[2] A triton is a single nucleus of tritium, which is an isotope of hydrogen containing two neutrons.

are given by Equations 1.1, 1.2, and 1.3 below, with the energies of their associated products indicated in parentheses.

$$^2D +^3 T \rightarrow^4 He(3.5MeV) + n^0(14.1MeV) \tag{1.1}$$

$$^2D +^3 He \rightarrow^4 He(3.6MeV) + p^+(14.7MeV) \tag{1.2}$$

$$p^+ +^{11} B \rightarrow (3)^4He(2.9MeV) \tag{1.3}$$

Deuterium-tritium (D-T) fusion, as shown in Equation 1.1, can be used as an example to demonstrate the scale of the problem of fusion energy production. The products of one D-T fusion reaction carry a combined total kinetic energy of 17.6 MeV, or 17.6 million electron-volts[3]. This is roughly equivalent to $1.6 \cdot 10^{-13}$ Joules. To put this value into perspective, producing enough power to operate a typical 60-watt household lightbulb would require approximately 21.3 trillion D-T fusion reactions per second. For comparison, the CERN Large Hadron Collider is capable of producing 600 million precisely head-on collisions between nuclei per second. This means that the largest, most advanced facility produced by the human race with the explicit goal of creating carefully directed high-energy collisions between atomic nuclei would only be capable of powering up to 0.002% of a lightbulb if it were repurposed to serve as a fusion powerplant.

In pursuit of nuclear fusion as a viable replacement for fossil fuel power, it is clear that arranging a discrete number of perfect collisions is not practical. Instead, it appears much more feasible to confine some mass of fusion reactants within some volume, and subject the reactants to some set of conditions which encourage fusion reactions to occur at some sufficiently high rate. For this, humanity must look to the example of the Sun. The Sun is a massive ball of plasma which produces energy through a sequence of fusion reactions known

[3] 1 eV is a unit of energy equivalent to the kinetic energy gained by an electron as it is accelerated through 1 volt of electric potential difference.

as the proton-proton chain reaction. This chain reaction involves the fusing of 4 protons into 1 alpha particle, outputting a total energy of approximately 26.7 MeV [7], through a series of intermediate reactions. The conditions within the Sun which enable a sufficiently high rate of fusion reactions are the temperature and density of the plasma in the solar core. Higher densities mean particles are closer together, and will therefore collide with each other more frequently. Positively charged nuclei repel each other through electrostatic forces, so a fusion reaction requires a collision energy great enough to overcome these forces. Higher temperatures mean higher velocities of random thermal motion between particles, which means a larger fraction of collisions between nuclei will occur with sufficient energies to fuse. To summarize, the Sun teaches us that higher densities and temperatures within a given volume of plasma will result in more fusion reactions per unit time within that volume of plasma.

The Sun achieves high plasma densities through gravitational confinement, meaning the solar mass alone provides sufficient force to prevent the plasma from expanding due to thermal pressure. Since gravity cannot be produced artificially, terrestrial power applications require a different method of confinement. The temperatures required to facilitate fusion reactions dwarf the melting points of even the most robust refractory metals, so solid material boundaries are not possible to enforce confinement. Therefore, the problem of facilitating terrestrial fusion becomes the problem of heating and confining a plasma to high temperatures and densities without physically touching it.

1.1.3 Thermonuclear Fusion: Magnetic Confinement of a Plasma

The nature of interactions between charged particles poses the main obstacle to nuclear fusion reactions. Ironically, this obstacle points towards a solution for fusion plasma confinement: a plasma can be manipulated without physical contact with solid boundaries through the use of electromagnetic forces.

The electromagnetic force, or the Lorentz force, can be observed at the macroscopic scale with the elementary example of two parallel, current-carrying wires in close proximity to each other. If the wires carry currents in the same direction, they will experience an attractive force between each other. If they carry currents in opposite directions, they will experience a repulsive force away from each other. This force is due to the sum of the forces acting on the charged particles in motion within the wire. Addressed at the scale of individual charged particles, the Lorentz force acting on a point charge is given by Equation 1.4, where q is the charge value, $\vec{v}$ is the velocity of the charge, and the electric and magnetic fields acting on the charge are $\vec{E}$ and $\vec{B}$, respectively.

$$\vec{F} = q(\vec{E} + \vec{v} \times \vec{B}) \tag{1.4}$$

1.2 The Z-Pinch

A classical Z-pinch is a self-confining plasma configuration which can heat and compress itself using only one power supply. The physical processes involved can be thought of as analogous to the mutual attraction in a bundle of wires carrying parallel currents. A cylindrical column of plasma subjected to an axial electric field will carry an electrical current in the axial direction. This current results in a magnetic field which wraps azimuthally around the plasma column. At all points within the plasma, the vector cross product between the axial electric field and the azimuthal magnetic field is oriented such that the Lorentz force is directed inwards towards the center axis of the column. The Lorentz force "pinches" the plasma inward, compressing and confining the column, while the plasma is ohmically heated by the current. Equilibrium in a Z-pinch occurs when radially inward magnetic pressure due to the Lorentz force balances the radially outward thermal pressure due to the plasma temperature. This radial force balance equilibrium is described in Equation 1.5 [8].

$$\frac{B_\theta}{\mu_0 r}\frac{d(rB_\theta)}{dr} = -\frac{dp}{dr} = -\frac{d}{dr}(nk(T_e + T_i)) \tag{1.5}$$

1.2.1 The Rayleigh-Taylor Instability

Unfortunately, the classical Z-pinch is highly suceptible to magnetohydrodynamic instabilities as the plasma approaches temperatures and densities required for fusion. These instabilities cause the pinch to collapse completely within a timescale on the order of 100 nanoseconds [9], [10]. These instabilities are due to Rayleigh-Taylor behaviors in the plasma structure [11]. Rayleigh-Taylor instabilities will occur at an interface between two fluids of different densities, where the low-density fluid exerts a force on the high-density fluid [12]. In other words, Rayleigh-Taylor instabilities occur in fluids where the pressure and density gradients are antiparallel. The radial force balance equilibrium given in Equation 1.5, known as the Bennett pinch relation, is combined with Ampere's law to predict radial equilibrium profiles of pressure and magnetic field [13]. The magnetic field profile is given in Equation 1.6 and the pressure profile is given in Equation 1.7, where I is the total pinch current and a is the characteristic pinch radius [14].

$$B_\theta(r) = \frac{\mu_0 I}{2\pi} \frac{r}{r^2 + a^2} \tag{1.6}$$

$$p(r) = \frac{\mu_0 I^2}{8\pi^2} \frac{a^2}{(r^2 + a^2)^2} \tag{1.7}$$

It has been empirically determined that the radial density profile in a Z-pinch can be closely approximated as a Lorentzian curve, as given by Equation 1.8, where n_0 is some maximum density at the center axis of the pinch [15].

$$n(r) = \frac{n_0 a^2}{r^2 + a^2} \tag{1.8}$$

It can be seen that Equation 1.8 shows a maximum density at the center of the pinch, and Equation 1.6 shows a maximum magnetic field at some finite radius r outside of the center. In the dynamic case of an imploding Z-pinch, this demonstrates that the compression of the pinch by the Lorentz force involves the low-density plasma at the edge of

the pinch accelerating inwards towards the high-density plasma at the center of the pinch resulting in Rayleigh-Taylor instabilities. Even in the case of a static equilibrium, where there is no appreciable net acceleration of the fluid interface, Rayleigh-Taylor instabilities are still driven by the antiparallel density and total pressure gradients at some radius where inward magnetic pressure $P_B = \frac{B^2}{2\mu_0}$ sufficiently exceeds hydrostatic thermal pressure $p(r)$ as described in Equation 1.7.

These instabilities grow rapidly, resulting in two dominant types of unstable pinch behavior. These behaviors, illustrated in Figure 1.1, are referred to as the m=0 sausage mode, and the m=1 kink mode [1].

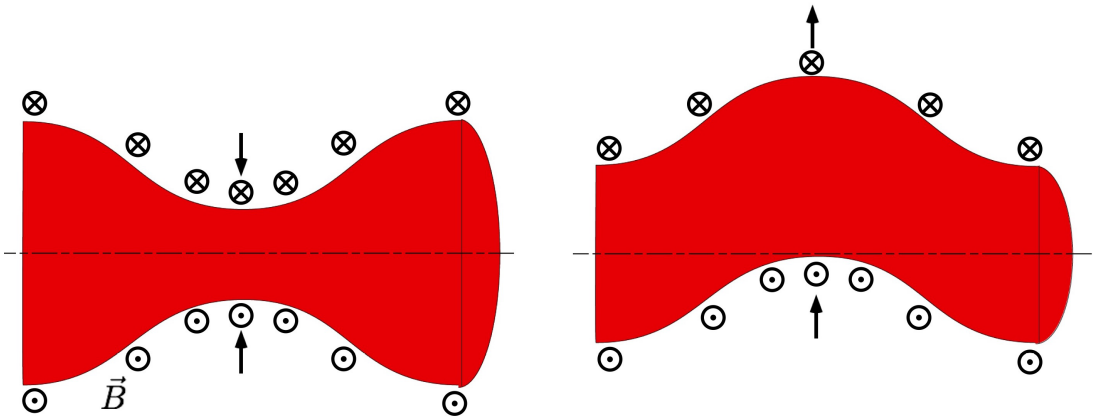

Figure 1.1: Left: the m=0 "sausage" mode occurs when one section along the length of the pinch is compressed to a tighter radius than the rest of the pinch. Right: the m=1 "kink" mode occurs when one section along the length of the pinch is radially displaced away from the pinch center axis. [1]

The two macroscopic instabilities shown in Figure 1.1 will grow exponentially in a classical Z-pinch, causing total loss of plasma confinement, making the Z-pinch an unfavorable choice for a thermonuclear fusion confinement configuration.

1.2.2 Sheared Flow Stabilization

The sausage and kink instabilities which prohibitively limit the confinement times of the classical Z-pinch at high energy densities can be mitigated by the application of a radially sheared axial velocity, such that the lower-density plasma at the edge of the pinch is moving faster than the higher-density plasma at the pinch center [16]. For effective stabilization against the m=1 kink mode, a radial velocity shear gradient exceeding the threshold defined in Equation 1.9 is required [17].

$$\frac{dV_z}{dr} \geq 0.1kV_A \tag{1.9}$$

This minimum shear gradient described in Equation 1.9 depends on the Alfven speed V_A and an assumed characteristic wave number k for the kink instability. The Alfven speed is calculated assuming maximum magnetic field B_0 and mass density ρ_0 as shown in Equation 1.10, and the kink wavenumber is inversely proportional to the pinch radius r as shown in Equation 1.11 [9].

$$V_A = \frac{B_0}{\sqrt{\mu_0 \rho_0}} \tag{1.10}$$

$$k = \frac{\pi}{r} \tag{1.11}$$

The application of this sheared flow has been demonstrated - both experimentally and by computational simulations - to extend the stable lifetime of a high energy density Z-pinch by multiple orders of magnitude to timescales exceeding 100 μs [18], [19], [20]. Experimental investigations of the sheared-flow-stabilized Z-pinch began in the early 2000's with the experimental device known as ZaP. The ZaP experiment served as an initial investigation of sheared flow stabilization, creating meter-long pinches at temperatures on the order of 100 eV and densities on the order of 10^{22} m^{-3}[17]. After a decade of experiments on ZaP-, the ZaP-HD device was created to examine scaling of the SFS Z-pinch to higher energy

densities. ZaP-HD forms 50 cm long pinches with typical temperatures around 600 eV and densities exceeding 10^{23} m^{-3} [1]. The FuZE device was later developed to produce the first actual SFS Z-pinch fusion reactions, with deuterium pinches exceeding densities of $5 \cdot 10^{23}$ m^{-3} and temperatures of 3 keV successfully generating neutrons in measurable quantities [21], [22], [23]. The most recent addition to the family of experimental SFS Z-pinch devices is known as FuZE-Q, and is intended to be the iteration which will achieve the milestone of scientific breakeven, or fusion gain $Q > 1$. The focus of this thesis is on measuring plasma densities in the ZaP-HD experiment.

Chapter 2

THE ZAP-HD EXPERIMENT

The success of the original ZaP experiment justified further investigation of the SFS Z-pinch. The logical next step was to build experiments of increasing power levels to study the scaling of SFS Z-pinch physics at higher energy densities. The first of these successive experiments is the ZaP-HD device, which has since been followed by FuZE and FuZE-Q. ZaP-HD is unique among these experiments in that it has three electrodes, as is shown in Figure 2.1. These three electrodes allow for the use of two separate power supplies: one for ionizing and accelerating the plasma, and one for compressing and heating the plasma. Decoupling the acceleration power from the confinement power enables higher pinch currents than were previously achievable in the ZaP experiment [1].

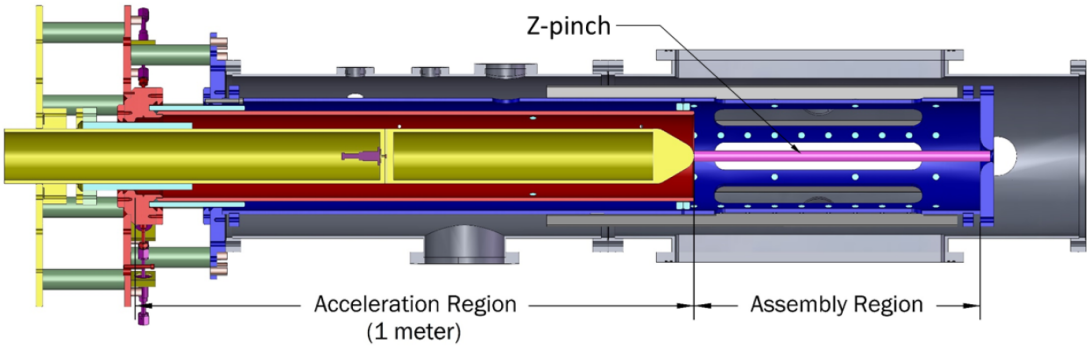

Figure 2.1: Cutaway diagram of the ZaP-HD device. This is a revolved image, the geometry should be viewed as concentric and cylindrical. In the given color scheme, the inner electrode is shown as yellow, the middle electrode is red, the outer electrode is blue, and the vacuum chamber boundary is gray. Plasma flows from left to right. The light dots seen on the outer electrode indicate the locations of magnetic field probes.

2.1 The Formation of a ZaP-HD Pinch

The process to form a ZaP-HD Z pinch begins with the injection of neutral gas into the vacuum chamber from two separate locations. The inner gas puff is a single valve inside the inner electrode which injects gas through 8 exhaust ports located 50 cm upstream of the nosecone. The outer gas puff consists of 8 valves which inject gas 95 cm upstream of the nosecone. The gas then expands within the space between the inner and middle electrodes. The timing of the gas injection is defined relative to the first power supply trigger. The inner and outer gas puff timings are controlled independently; a typical operational example of these timings is t=-1.4 ms for the inner and t=-0.8 ms for the outer. The total amount of gas injected is on the order of 20 milligrams.

At t=0, the first power supply, a 680 μF capacitor bank referred to as the "acceleration bank," discharges between the middle and inner electrodes at a voltage of up to 10 kV. This ionizes the injected gas, forming a current sheet, which is accelerated axially through the Lorentz force. The current sheet experiences a radially inward Lorentz force component as it reaches the nosecone, and the plasma forms a "snowplow" wavefront. After some delay (typically t=+20 μs) another 680 μF capacitor bank, the "compression bank," is triggered, applying a voltage between the outer and inner electrodes. The current sheet attaches to the outer electrode and collapses onto the machine center axis. A SFS Z pinch is formed, with an axial flow continuously fed by the residual gas left behind in the acceleration region by the initial snowplow. The pinch is compressed and heated until the capacitor banks are fully discharged [24]. This chronology of completing a single ZaP-HD "pulse" is represented illustratively in Figure 2.2. The approximate timescale of a ZaP-HD "pulse" is less than 150 μs.

2.2 Diagnostic Suite

The ZaP-HD experiment employs a variety of diagnostics to measure relevant plasma parameters. These diagnostics operate by observing emitted light from the plasma, probing

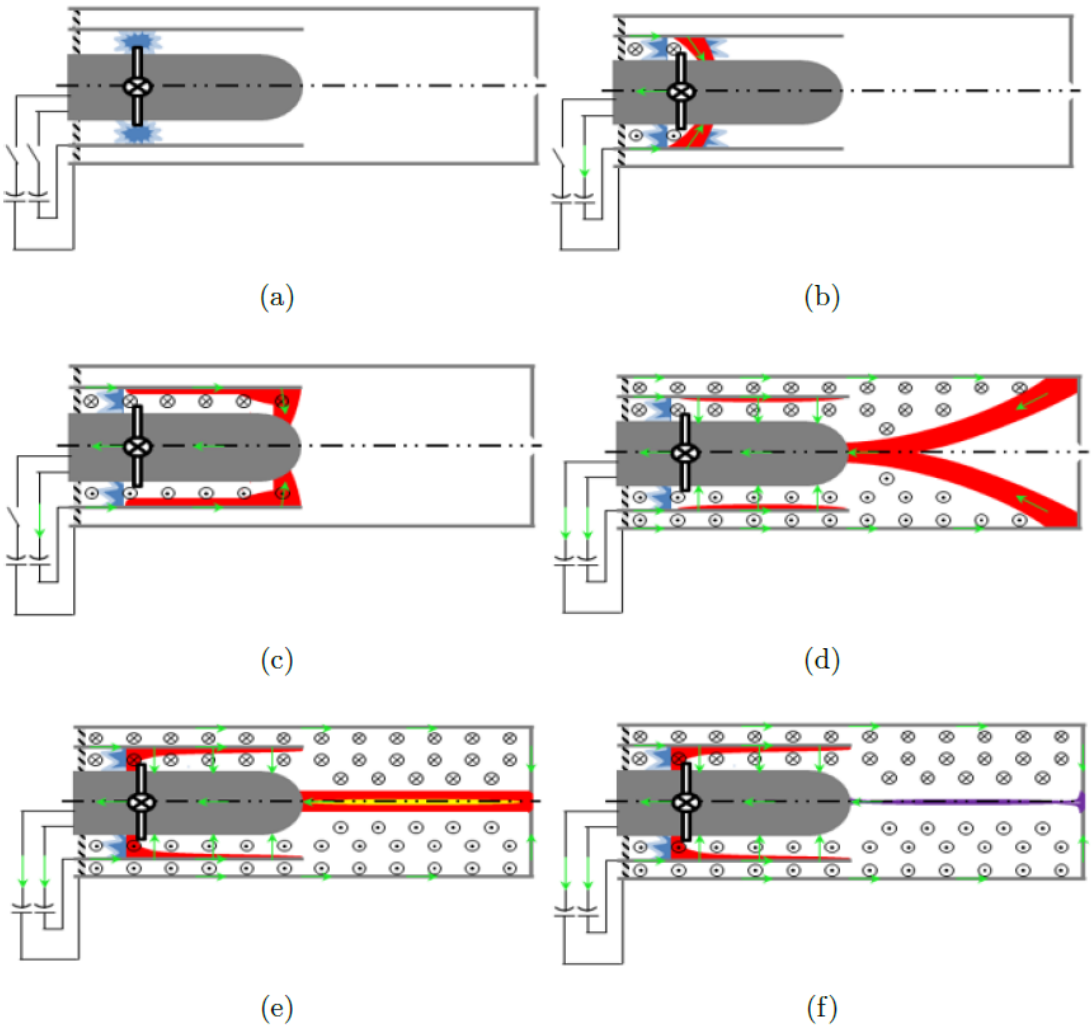

Figure 2.2: Illustrated chronology of a ZaP-HD Z pinch pulse. (a) Neutral gas is injected and permitted to expand within the annular gap between the middle and inner electrodes. (b) The acceleration bank applies a voltage between the inner and middle electrodes, ionizing the gas and forming a current sheet. The plasma is accelerated axially by the Lorentz force. (c) The plasma forms a snowplow wavefront as it approaches the end of the acceleration region. (d) The compression bank applies a voltage between the outer and inner electrodes, causing the plasma to collapse onto the center axis of the ZaP-HD device. (e) A SFS Z-pinch is formed, fed with flowing plasma from the residual gas left behind by the snowplow. (f) The pinch current compresses and heats the plasma.

the plasma with directed external light sources, and collecting induced currents in response to the plasma current. Collectively, these tools enable the characterization of localized and bulk-flow behaviors in the plasma.

2.2.1 Interferometry

Interferometry is a method of measuring the refractive index of a medium by measuring the interference experienced by a source of coherent light which has propagated through the medium being measured. The index of refraction of a plasma is directly proportional to the electron density of the plasma. This makes plasma interferometry a valuable tool for directly measuring electron density. The ZaP-HD experiment utilizes two different interferometry systems.

Digital Holographic Interferometry (DHI) records plasma densities at a fixed point in time by using a pulsed Nd:YAG laser to create a hologram on a digital camera sensor. The incident laser beam is expanded to a wide area to measure a section of plasma at a high spatial resolution.

Helium-neon (HeNe) interferometry records time-resolved plasma density curves for the duration of an entire ZaP-HD pulse using a continuous-wave gas tube HeNe laser which transmits interference signals to a photodiode. The incident laser beam is split into separate chords to provide measurements at multiple discrete points. This thesis revolves primarily around data collected using the HeNe interferometer, which will be covered in much greater detail in Chapter 3. A grossly oversimplified illustration of the HeNe interferometer concept is given in Figure 2.3.

Figure 2.3 depicts a simple single-chord Mach-Zehnder plasma interferometer setup. A HeNe laser beam is split into a “scene beam” which is used to probe the plasma, and a “reference beam” which is used to subtract out disturbances in the laboratory setting which

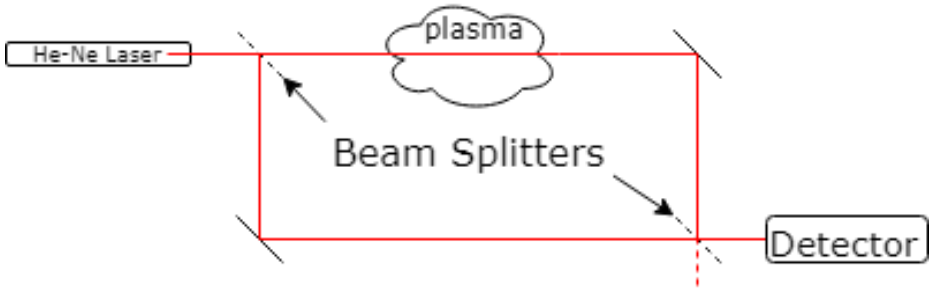

Figure 2.3: A basic depiction of a Mach-Zehnder HeNe interferometer chord. The laser beam is split into a scene beam and a reference beam. The scene beam passes through the plasma, and the reference beam follows a similar path outside of the experiment. The beams are recombined and directed into some form of detector, which measures the interference between the recombined beams.

do not come directly from the plasma. The beams are recombined and directed into a photodetector. The detector measures the time-dependent shift in the phase angle between the scene and reference beams, which is used to determine the time-dependent change in the index of refraction observed by the scene beam. Once again, this will be described in much greater detail in Chapter 3.

2.2.2 Rogowski Coils

Electrical currents through the separate acceleration and compression power supplies, as well as through the plasma as a whole, are measured using Rogowski coils. Rogowski coils are looped around a location of interest such that the current being measured flows in one direction through the plane of the loop, inducing a current through the Rogowski coil, resulting in a voltage between the two ends of the coil. This is shown in Equation 2.1, where N is the number of turns in the coil, L is the total length of the coil, and A is the coil area [1].

$$V_{output} = -\frac{d\Phi}{dt} = -\mu_0 \frac{N}{L} A \frac{dI}{dt} \tag{2.1}$$

Equation 2.1 shows that the voltage output of the coil is proportional to the derivative of the current being measured, so the signal is integrated and multiplied by some calibration factor to determine the final current measurement.

Within the scope of this thesis, current measurements taken using Rogowski coils are used to compare trends in pinch current to trends in electron density.

2.2.3 Magnetic Field Probes

The ZaP-HD experiment is equipped with circular arrays of "B-Dot" magnetic field probes positioned along the length of the outer electrode. This thesis is concerned with five azimuthal probe arrays, all located within the ZaP-HD assembly region. The assembly region contains a total of ten azimuthal probe arrays, four arrays having eight probes each and six arrays having four probes each. A diagram indicating the locations of the assembly region probe arrays is given in Figure 2.4. The locations of the five arrays of interest are Z = +15, 20, 25, 30, and 45 centimeters downstream of the middle electrode. The reasons for interest in these particular arrays are discussed in Chapter 4.

The B-dot probes function on a similar operating principal to the Rogowski coils. By Faraday's law, the magnetic field around the pinch changing in time will produce a voltage across the coils as described by Equation 2.2 [1].

$$V_{output} = -\frac{d\Phi}{dt} = -NA\frac{dB}{dt} \tag{2.2}$$

Notes on Arrays of Interest

The five arrays of interest for this thesis include three of the 8-probe arrays and two of the 4-probe arrays. The 8-probe arrays have probes spaced azimuthally at 45° intervals, and the 4-probe arrays are spaced at 90° intervals. At the time of experimentation conducted

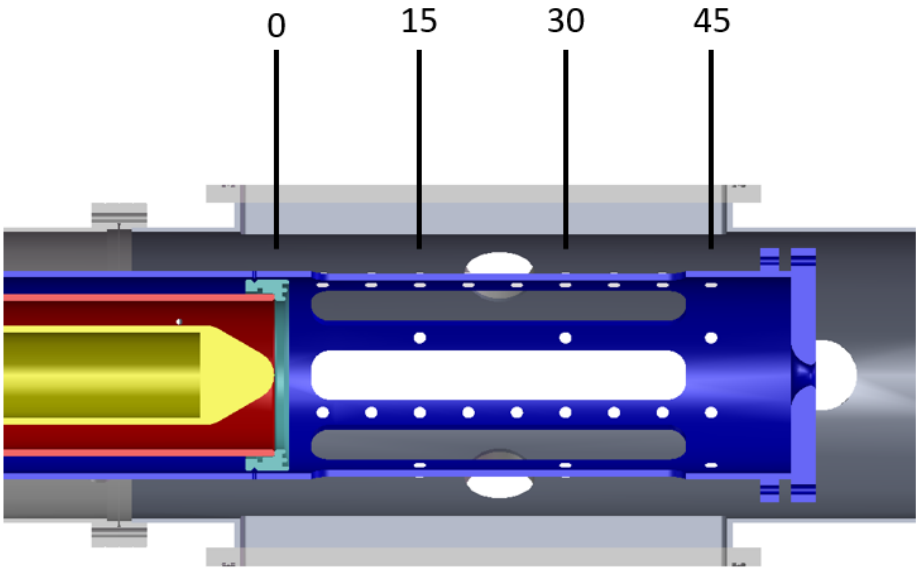

Figure 2.4: Assembly region diagram of ZaP-HD including B-dot probe arrays [1]. Probes are indicated by white circles. Numbers shown indicate locations of 8-probe azimuthal arrays in centimeters downstream of the end of the middle electrode. The 8-probe arrays are spaced 15 cm apart from each other, with 4-probe arrays spaced every 5 cm in between.

for this thesis, the 8-prove arrays at z = +15, 30, and 45 centimeters appear to function as normal. However, for the 4-probe arrays, the z = +20 cm location has two malfunctioning probes, and the z = +25 cm location has one malfunctioning probe. Consequences of the rsulting gaps in data are discussed in Chapter 4.

2.2.4 High Speed Imaging

A high-speed Kirana digital camera capable of capturing videos at up to 5,000,000 frames per second is used to record qualitative visual information on ZaP-HD plasmas. The Kirana only measures visible light, and ZaP-HD plasmas emit dominantly on the UV spectrum, so in reality the Kirana only images the cloud of hot, excited neutrals shrouding the pinch. However, this provides a useful source of pinch geometry visualization which can be used to interpret results from other diagnostics more intuitively.

2.2.5 Spectroscopic Measurements

Spectroscopy is a common tool used in plasma physics experiments to determine the temperature and velocity of ions. Bound electrons transitioning from excited states to lower energy states emit photons of discrete wavelengths. These wavelength emissions are well understood and extensively documented in the NIST Atomic Spectra Database [25]. The temperature of a plasma can be determined by the width of the Doppler-broadened wavelength distribution around a known center-band emission line. Similarly, the velocity of a bulk flow of plasma can be determined by the net shift in one direction of the center-band emission line, as ions moving away from the observer will produce a slight "redshift", or increase in wavelength, while ions moving towards the observer will produce a "blueshift," or a decrease in wavelength. One caveat to this subset of diagnostics is the fact that ZaP-HD operates on elemental hydrogen as fuel. Ionized hydrogen has no bound electrons, and therefore has no discrete line emissions. Therefore, spectroscopic measurements in ZaP-HD must rely on line emissions from heavier impurity ions, such as copper, tungsten, and car-

bon. This presents a third use for spectroscopy, determining impurity concentrations in the plasma flow by measuring the intensity of impurity line emissions.

2.2.6 In Development

Over a decade has passed since the ZaP-HD device produced its first Z pinch plasma, and there are still new physics investigations to be explored. New investigations require new diagnostics, one of which is currently under development at the University of Washington.

Pyrometry

The SFS Z-pinch is an open confinement configuration which requires solid electrodes to maintain physical contact with hot, dense plasmas. No known material can withstand such conditions without experiencing some form of erosion. Therefore, it is necessary to characterize the rate of surface erosion, and work towards achieving more thorough understanding of the conditions which the ZaP-HD electrodes are subjected to.

A design for a two-color pyrometer is being tested and refined for time-resolved measurements of the surface temperature of the ZaP-HD nosecone [26]. The pyrometer measures the average temperature over the surface area from which radiation is observed. The area of observation is tuned using a fiber-coupled lens to a spot size as small as 1 cm^2 to enable spatially localized measurements of different points on the nosecone surface. Unlike a typical optical thermometer, the two-color system is robust against variations in material emissivity.

Chapter 3

THE HELIUM-NEON INTERFEROMETER

Interferometry is a broad collection of techniques which use the observed interference between superimposed waves to measure properties of a physical system. This thesis is concerned with the use of heterodyne quadrature interferometry to record temporally resolved measurements of the electron density in a ZaP-HD plasma. The interferometer is set up in a Mach-Zehnder configuration with unequal path lengths, and uses a helium-neon (HeNe) gas tube laser as a light source.

This chapter details the theory behind the interferometry diagnostic, including standard simplifying assumptions for plasma interferometry as well as information specific to the configuration used on ZaP-HD. The physical laboratory setup is discussed, as are the signal analysis techniques used to determine electron density measurements.

3.1 Introductory Example: the Basic Mach-Zehnder Interferometer

Before diving into every niche detail of the interferometer used on ZaP-HD, it is helpful to explain the functionality of a basic Mach-Zehnder configuration. This configuration was briefly introduced in Figure 2.3 in Section 2.2.1. A more explicitly annotated version of this diagram is presented in Figure 3.1.

To operate the interferometer as shown in Figure 3.1, one would begin recording the detector output before any plasma is created. The detector is an amplified photodiode, which outputs a voltage waveform. This waveform contains information on the time-dependent phase shift $\Delta\phi(t)$ between the scene and reference beams. Beginning to record this waveform several plasma lifetimes before any plasma is created provides information on how

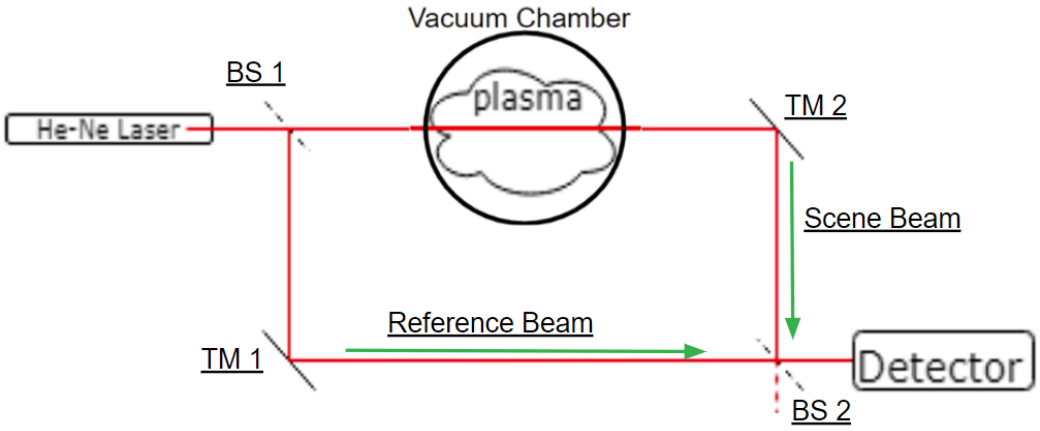

Figure 3.1: Annotated diagram of a basic Mach-Zehnder interferometer. The beam splitter "BS 1" splits the laser into a "scene beam" and a "reference beam." The scene beam probes the plasma, and is directed downwards by turning mirror "TM 2." The reference beam is diverted around the experiment entirely by turning mirror "TM 1.". The two beams are recombined by beam splitter "BS 2," and the recombined beam is sent into the detector.

ambient noise in the laboratory affects $\Delta\phi(t)$. The experiment would then be triggered, and $\Delta\phi(t)$ would continue being recorded throughout the duration of the plasma pulse. After the plasma dissipates, the recording of $\Delta\phi(t)$ would then continue for several more plasma lifetimes as $\Delta\phi(t)$ returns to ambient baseline behavior.

3.2 Theory of Operation: the Ordinary Wave

Section 3.1 provided an operational example of how a photodetector in a Mach-Zehnder interferometer would output a waveform containing the phase shift $\Delta\phi(t)$ between the scene and the reference beam. Before moving onto the specifics of how exactly $\Delta\phi(t)$ is measured, it makes sense to explain why $\Delta\phi(t)$ is important.

The electron density of a plasma is directly related to the refractive index experienced by a wave propagating through the plasma. Therefore, measuring the index of refraction

observed by a laser propagating through a plasma may reveal the electron density integrated along the length of the path of the laser through the plasma. Measurements of this refraction are connected to electron density through a dispersion relation. For plasma interferometry, it is common practice to assume the dispersion relation for the O-wave, or the ordinary wave [27].

Several simplifying assumptions are required to arrive at the O-wave dispersion relation. The O-wave exclusively describes electromagnetic electron wave behavior, so the first assumption to be made is that the laser exclusively interacts with electrons, and ion motion can be neglected. This assumption is reasonable, as hydrogen ions are over 1800 times more massive than electrons. Therefore, the electrons are sufficiently mobile to respond to the laser frequency, but the heavier ions in the plasma are too slow to respond.

The O-wave is derived from the Cold Plasma Dispersion Relation (CPDR), so another necessary assumption to be made is that the plasma being measured is "cold." This assumption may sound strange for a fusion experiment, as one goal of such experiments is typically to pursue high plasma temperatures. However, for electron wave dispersion behavior to be modified by thermal effects to a noticeable degree, the temperature of a plasma must be high enough for electron thermal velocities to be comparable to the speed of light [28].

These assumptions lead to the use of the Appleton-Hartree relation to describe the index of refraction, as shown below in Equation 3.1.

$$N^2 = 1 - \frac{X(1-X)}{1 - X - \frac{1}{2}Y^2 sin^2\theta \pm \sqrt{(\frac{1}{2}Y^2 sin^2\theta)^2 + (1-X)^2 Y^2 cos^2\theta}} \tag{3.1}$$

The constituent terms of the Appleton-Hartree equation are given below in Equations 3.2, 3.3, 3.4, and 3.5.

$$\omega_p = \sqrt{\frac{n_e e_c^2}{\epsilon_0 m_e}} \tag{3.2}$$

$$X = \frac{\omega_p^2}{\omega^2} \tag{3.3}$$

$$\omega_c = \frac{e_c B_0}{m_e} \tag{3.4}$$

$$Y = \frac{\omega_c}{\omega} \tag{3.5}$$

Relevant variables and constants are defined as follows:

- Frequency of propagating wave: ω
- Wavenumber of propagating wave: k
- Elementary charge: e_c
- Permittivity of Free Space: ϵ_0
- Electron mass: m_e
- Angle between direction of wave propagation and background magnetic field: θ
- Electron plasma frequency: $\omega_p = \sqrt{\frac{n_e e^2}{\epsilon_0 m_e}}$
- Normalized plasma frequency: $X = \frac{\omega_p^2}{\omega^2}$
- Electron cyclotron frequency: $\omega_c = \frac{eB_0}{m_e}$
- Normalized cyclotron frequency: $Y = \frac{\omega_c}{\omega}$

Equation 3.1 provides the dispersion relation for electromagnetic electron waves in a cold plasma. There are four waves which fall into this category: the O, X, L, and R waves. To justify ignoring the behaviors of the L and R waves, which correspond to circular light polarization, it is assumed that the strength of the component of the magnetic field which is parallel to the direction of scene beam propagation is negligible. This is reasonable due to the short path length of the scene beam through the plasma (order of 1 cm) and the geometry of the pinch ensuring that the path with the strongest parallel magnetic field must correspond to the shortest possible path length (the longest path would be through the center of the pinch, and therefore only see perpendicular magnetic fields). Neglecting X-wave behaviors is reasonable due to the high frequency of the laser, as the wave frequency would need to be much closer to the cutoff frequency ω_c given by Equation 3.10 for the X-wave behaviors to differ considerably from the O-wave. These considerations allow the simplification of Equation 3.1 to Equation 3.6, which is the O-wave dispersion relation.

$$N^2 = 1 - X \tag{3.6}$$

Equation 3.6 simplifies further to provide the O-wave index of refraction, as given by Equation 3.7.

$$N = \sqrt{1 - \frac{\omega_p^2}{\omega^2}} \tag{3.7}$$

It is not expected for electron density in ZaP-HD to exceed the order of 10^{23} electrons per cubic meter, which means that the plasma frequency in ZaP-HD should not exceed the order of single-digit terahertz. The frequency of a 632.8 nm HeNe laser is approximately 474 terahertz. Therefore, $\omega >> \omega_p$, which allows Equation 3.7 to simplify to Equation 3.8.

$$N = 1 - \frac{\omega_p^2}{2\omega^2} \tag{3.8}$$

Equation 3.8 provides the index of refraction in terms of plasma frequency and electromagnetic wave frequency. To extract electron density from the plasma frequency, it is helpful to expand the electromagnetic wave frequency into terms of the O-wave cutoff density n_c, or the electron density at which waves of frequency ω will no longer propagate through the plasma, and instead be reflected. The cutoff density n_c is given by Equation 3.9.

$$n_c = \frac{4\pi^2 c^2 m_e \epsilon_0}{\lambda_{laser}^2 e_c^2} \tag{3.9}$$

Plugging n_c as described by Equation 3.9 into Equation 3.2 leads to the expression of laser frequency in terms of the cutoff density as given in Equation 3.10, which allows Equation 3.8 to be rewritten as Equation 3.11.

$$\omega = \sqrt{\frac{n_c e_c^2}{m_e \epsilon_0}} \tag{3.10}$$

$$N = 1 - \frac{n_e}{2n_c} \tag{3.11}$$

Equation 3.11 is significant as it describes the index of refraction of the plasma purely in terms of electron density n_e and the constant known cutoff density n_c which is defined by the HeNe laser. Now that the index of refraction has been defined in desirable terms, it must be connected to the phase shift which will be directly measured by the interferometer. The phase lag ϕ experienced by a laser beam is given by Equation 3.12, where c is the speed of light.

$$\phi = \int k dl = \int N \frac{\omega}{c} dl \tag{3.12}$$

It is important to note that the $\int dl$ integral in the phase lag ϕ described by Equation 3.12 means that the index of refraction N contributing to the total phase lag is integrated over the entire path of the beam, without regard for what portions of that path contain

plasma. This demonstrates the importance of the split into a scene beam and reference beam, to allow the index of refraction of the plasma to be separated from the rest of the refraction experienced by the beam. This separation is described by Equation 3.13, which expresses the difference in phase angle between the scene and reference beam in terms of the difference in refractive index between the plasma and the surroundings.

$$\Delta\phi = \int (k_{plasma} - k_0) dl = \int (N-1)\frac{\omega}{c} dl \tag{3.13}$$

Substituting Equation 3.11 into Equation 3.13 yields Equation 3.14.

$$\Delta\phi = \int (1 - \frac{n_e}{2n_c} - 1)\frac{\omega}{c} dl = -\int (\frac{n_e}{2n_c})\frac{\omega}{c} dl \tag{3.14}$$

Removing the constants from the integral and applying $c = \lambda\omega/2\pi$ gives Equation 3.15.

$$\Delta\phi = -\frac{\pi}{n_c\lambda}\int n_e dl \tag{3.15}$$

Substituting known values for the constants in Equation 3.15, and removing the negative as the phase difference $\Delta\phi$ can be thought of as an absolute value and negative densities would be physically impossible, one arrives at Equation 3.16, an expression which provides the chord integrated electron density as a simple linear function of $\Delta\phi$.

$$5.61 \cdot 10^{20}\Delta\phi = \int n_e dl = N_e \tag{3.16}$$

The symbol N_e will from here on be used to describe the "chord integrated electron density," which refers to the electron density integrated along the path length of the scene beam through the plasma. This density is in units of electrons per square meter. Obtaining a volumetric density in the more intuitive and useful units of electrons per cubic meter requires dividing N_e by some assumed length, or deconvolving values of N_e with respect to

each other as measured by multiple adjacent, parallel chords of known spatial separation.

Equation 3.16 is significant, as it relates the time-dependent phase shift $\Delta\phi(t)$ to the electron density of the plasma by a simple conversion factor. This demonstrates the importance of measuring $\Delta\phi(t)$. Now that this relationship has been established, it makes sense to move on into the details of how exactly $\Delta\phi(t)$ is measured on ZaP-HD.

3.3 Heterodyne and Quadrature Signal Processing

As mentioned in the previous section, the HeNe laser has a frequency of 474 terahertz, corresponding to an oscillation period of roughly 2 femtoseconds ($10^{-15}s$). The author is unaware of whether a photovoltaic sensor capable of femtosecond response times exists. However, the author does know that such an exotic device would be out of budget for this thesis project, so the speed of the signal being measured must be reduced to a more manageable order of magnitude. This is accomplished through heterodyning.

In the context of this thesis, heterodyning refers to elevating the reference beam to a slightly higher frequency than the scene beam, such that a known beat frequency is imposed on the recombined beams. This enables the time-dependent phase shift in the scene beam to be measured on much more reasonable timescales.

The HeNe interferometer used on ZaP-HD employs a 40 MHz heterodyne signal produced by a typical function generator. This 40 MHz signal is sent to an Acousto-Optic Modulator (AOM for short, also known as a "Bragg cell") to impose the frequency shift on the reference beam.

The Bragg cell consists of an acoustic oscillator and an optical crystal, and replaces the first beam splitter (labeled "BS 1" in Figure 3.1) in a typical Mach-Zehnder interferometer setup. The HeNe laser beam passes through the crystal as it is subjected to 40 MHz vibrations. Approximately 90% of the beam power remains in the unchanged zeroth order

diffraction, which is used as the scene beam. Approximately 10% of the beam power is converted to the first order diffraction, with a frequency 40 MHz greater than the original beam, and is used as the reference beams. Higher order diffractions account for negligible power fractions and do not escape the housing of the AOM. The 90/10 power split is a design parameter of the specific Bragg cell used on ZaP-HD, and is not inherent to all Bragg cells.

Heterodyning maps the information of the time-dependent phase shift $\Delta\phi(t)$ onto an easily measured 40 MHz waveform. To extract an actual measurement of $\Delta\phi(t)$ from this waveform, a signal processing technique known as "quadrature" is used. On ZaP-HD, quadrature involves splitting the photodetector output waveform into components which are 90° out of phase with each other, then mixing these components with a clean 40 MHz reference signal from the same function generator which drives the Bragg cell. The result is two output waveforms, which can be regarded as the sine and cosine of $\Delta\phi(t)$.

The analog electronics which detect the 40 MHz heterodyned waveform and perform the quadrature processing to decompose the signal into $sin(\Delta\phi(t))$ and $cos(\Delta\phi(t))$ are discussed in detail in Section 3.4.

3.4 Analog Signal Processing

This section covers the two distinct subsystems of the HeNe IF data collection circuitry. First, a photodetector which receives the recombined laser beams and outputs a voltage. Next, an assortment of "mixer-splitter" radiofrequency processing electronics which compares the voltage output from the photodetector to the 40 MHz heterodyne reference signal output from the function generator to separate the measured phase shift into sine and cosine components.

3.4.1 Photodetector Circuit

The photodetector circuit contains four components of significant interest: a photodiode, a buffer amplifier, a notch filter, and a TIA (transimpedance amplifier). The photodiode is reverse biased by a 45 volt battery. This relatively high reverse bias voltage gives the photodiode a rise time on the order of 1 ns. This enables the measurement of the heterodyne signal in compliance with the Nyquist criteria, as the 40 MHz signal has a period of 25 ns. The photodiode drives a current, producing a voltage which is measured by the buffer amplifier. The buffer amplifier, also commonly referred to as a unity gain amplifier, outputs the input voltage received from the photodiode at a more favorable impedance. The output from the buffer amplifier passes through an LC "notch" band-pass filter. This filter has a resonant passband frequency of 40 MHz to allow the desired heterodyne signal to pass through, while attenuating other unwanted frequencies to reduce noise. The signal leaving the passband is input into the transimpedance amplifier, which increases the magnitude of the signal. The gain of the transimpedance amplifier is adjusted by a potentiometer.

The electric field components of the superimposed scene and reference beams are given by Equations 3.17 and 3.18, respectively [27].

$$E_{scene} = A_s e^{i(\omega t + \phi(t))} \tag{3.17}$$

$$E_{reference} = A_r e^{i(\omega + \omega_{AOM})t} \tag{3.18}$$

These superimposed electric fields interact with the photodiode, driving a proportional current. This current is converted to a voltage by the buffer amplifier. The voltage is then filtered and the amplified by the TIA. The TIA outputs a voltage which can be expressed as Equation 3.19.

$$V_{TIA} = C \cdot A_s A_r cos(\Delta\phi(t) - \omega_{AOM} t) \tag{3.19}$$

Where C is some scaling constant depending on the responsivity and quantum efficiency of photodiode. It should be noted here that the absolute magnitudes of the electric fields E_{scene} and $E_{reference}$, the amplitudes A_s and A_r, and the constant C here are all unknown constants, and are given here purely to demonstrate how the observed waveform changes as it moves through the analog electronics. The voltage output V_{TIA} is sent to the mixer-splitter electronics for quadrature processing.

3.4.2 Mixer-Splitter Electronics

The photodetector transimpedance amplifier output waveform V_{TIA} is sent to the input of the 90° power splitter of the mixer-splitter circuit shown in Figure 3.2. The 90° power splitter splits the power of the signal in half, and delays one of the two halves by a phase angle of 90°. These two halves are then sent to signal mixers, where they are combined with clean 40 MHz signals from the function generator.

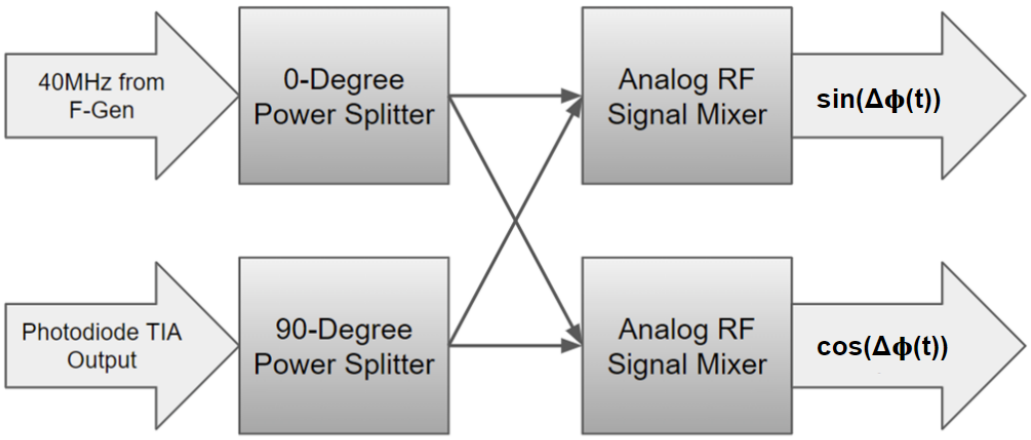

Figure 3.2: Block diagram of the mixer-splitter electronics employed by the ZaP-HD interferometer.

The outputs of the mixer-splitter box as shown in Figure 3.2 are the sine and cosine

components of the time-dependent phase shift $\Delta\phi(t)$. These are the final analog signal outputs of the interferometer. These signals are digitized by Lecroy TR3412 transient recorders in the ZaP-HD data acquisition system and stored for post-processing.

3.4.3 Visualizing $\Delta\phi(t)$: The Lissajous Figure

It is helpful to visualize the mixer-splitter output data by plotting a Lissajous figure. To form a Lissajous figure, mixer-splitter box outputs are plotted against each other on a 2-D coordinate plane. Since these outputs are essentially the same waveform separated by a 90° phase angle, this plot will trace a circular arc as the sample time progresses. This can be thought of as tracing $\Delta\phi(t)$ around the unit circle.

As mentioned in Section 3.1, even without any plasma present, a phase shift can be observed and recorded due to ambient mechanical vibrations in the laboratory. This vibrational phase shift results in a full circle being traced on a Lissajous figure every few milliseconds. This Lissajous is used as a tool to verify proper laser alignment. While setting up an interferometer chord, the mixer-splitter outputs $sin(\Delta\phi(t))$ and $cos(\Delta\phi(t))$ are plotted in real-time on an oscilloscope, as shown in Figure 3.3. Optics are adjusted to maximize the radius of the Lissajous figure.

3.5 Multichord Operation

As mentioned earlier, a level of spatial resolution is achieved by operating the interferometer with multiple chords. One "chord" refers to one scene and reference beam pair employed to record a density measurement at one specific location in the plasma. The ZaP-HD interferometer is currently equipped to operate with up to four chords. A simplified illustration demonstrating a two-chord setup is given in Figure 3.4.

The diagram provided in Figure 3.4 is modified from a diagram of the interferometer used on the FuZE experiment [27]. This diagram depicts a planar beam splitter being used to

Figure 3.3: Three photographs of oscilloscopes outputting Lissajous figures. From left to right, the figures represent a misaligned chord, a poorly aligned chord, and a properly aligned chord. The misaligned chord shows no circular arc. The poorly aligned chord shows a fuzzy circle of approximately 5 millivolt radius. The properly aligned chord shows a defined circle of approximately 40 millivolt radius.

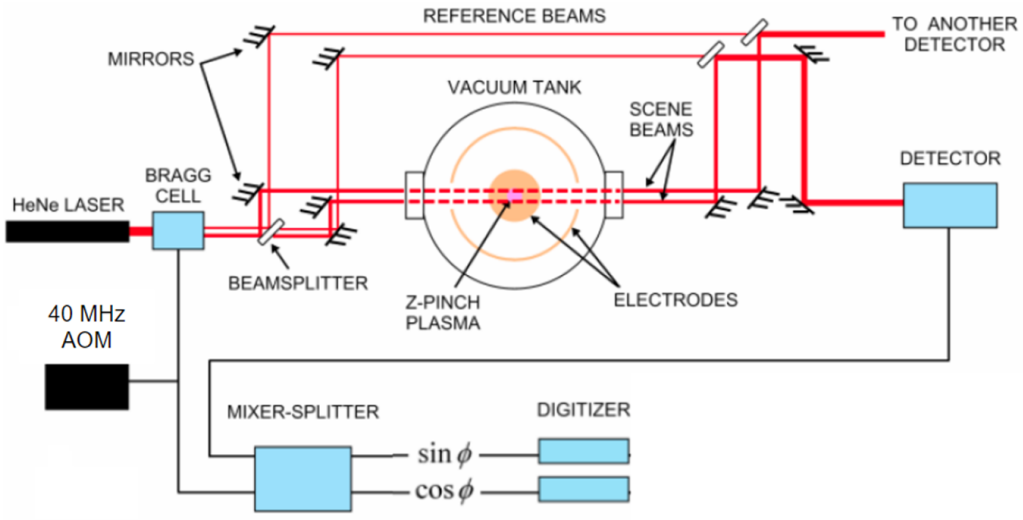

Figure 3.4: Graphical representation of the ZaP-HD multichord interferometer. Only two chords are shown for simplicity. The scene and reference beam outputs from the Bragg cell are split into multiple chords using beam splitters.

divide one chord into two chords. The setup used on ZaP-HD for this thesis employed three cubic beam splitters to divide the Bragg cell outputs into four chords, as shown in Figure 3.5.

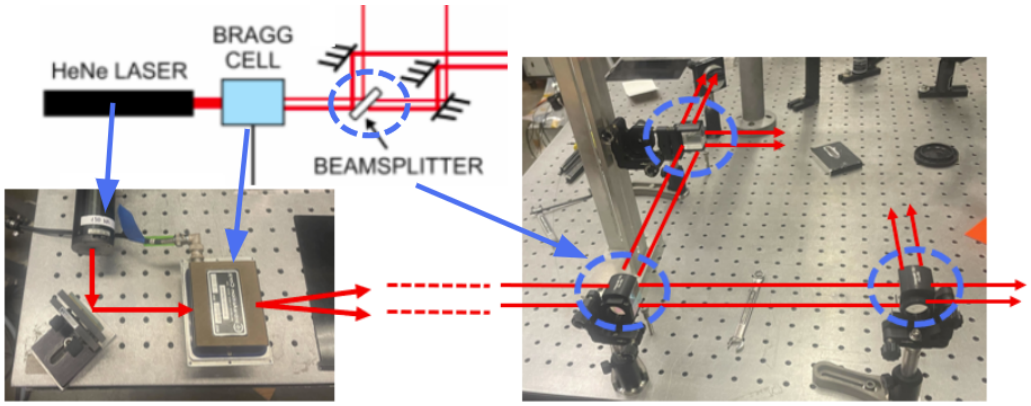

Figure 3.5: Annotated photographs showing the cube splitters used to divide the Bragg cell outputs into four chords on the ZaP-HD interferometer.

3.6 Digital Post-Processing

Once the mixer-splitter outputs of $sin(\Delta\phi(t)$ and $cos(\Delta\phi(t)$ are obtained, post-processing tasks are required to determine the phase shift $\Delta\phi(t)$. The three primary tasks are offset subtraction, fringe jump subtraction, and vibration subtraction. These tasks contribute to determining $\Delta\phi(t)$ by enabling the continuous unwrapping of the arctangent of the mixer-splitter outputs by Equation 3.20.

$$\Delta\phi(t) = \arctan(\frac{\sin\Delta\phi(t)}{\cos\Delta\phi(t)}) \tag{3.20}$$

3.6.1 Offset Subtraction

Due to finite tolerances in the manufacturing of the photodetectors and the mixer-splitter circuitry, the Lissajous figure is never recorded as perfectly centered on the origin. For con-

sistent phase shift unwrapping, the center offset from the origin must be subtracted. This is done by curve fitting a circle to the Lissajous figure, and subtracting the center coordinates of that circle from the recorded data. Figure 3.6 provides an example demonstrating this operation.

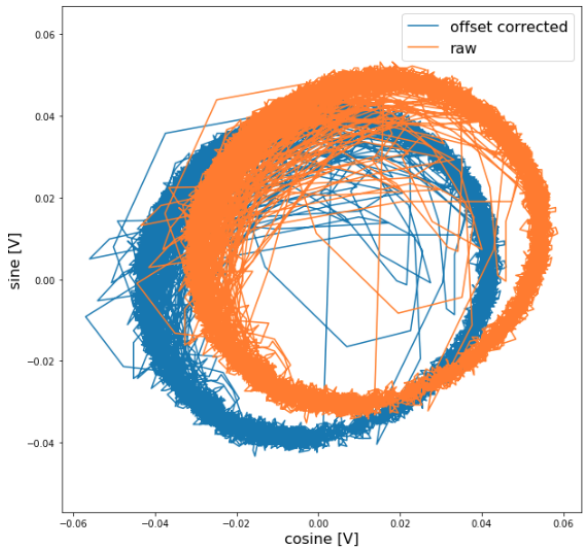

Figure 3.6: Two Lissajous figures overlaid on the same axes. Orange is before offset subtraction, blue is after offset subtraction.

Due to thermal drift occurring in the analog circuitry throughout the course of a full day of experimentation, it is insufficient to calculate a single baseline offset subtraction which is applied to all pulses. Therefore, the operation depicted in Figure 3.6 must be performed once per chord, per plasma pulse.

3.6.2 Fringe Jump Subtraction

While the desired measurement of the interferometer is the time-dependent phase shift $\Delta\phi(t)$, it is important to remember that the directly measured signals from the mixer-splitter electronics are voltage waveforms, rather than direct angular measurements. These

waveforms do not differentiate between rotations around the unit circle. Therefore, the unwrapping of the arctangent described in Equation 3.20 occurs within periodic boundary conditions at $\Delta\phi(t) = 0$ and $\Delta\phi(t) = 2\pi$. This results in a "fringe jump," or a jump in the $\Delta\phi(t)$ signal to the opposite boundary condition, at each interval of 2π. This corresponds to crossing between quadrant one and quadrant four on the unit circle, in either direction, as depicted in Figure 3.7.

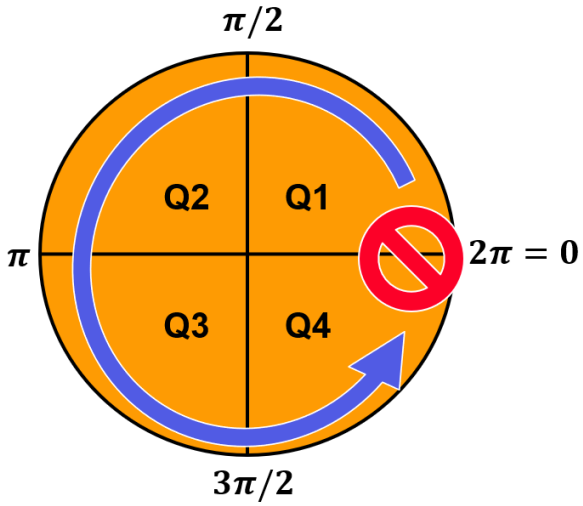

Figure 3.7: A graphic depicting the location of the periodic discontinuity in the unwrapping of the arctangent of the mixer-splitter outputs. Fringe jumps occur when crossing this discontinuity in both the positive and negative direction.

In the vibrational signal, with no plasma present, such a fringe jump will typically occur every 1-2 milliseconds. An example of such a fringe jump is shown in Figure 3.8.

During a ZaP-HD pulse taken in the upper range of operating powers, it is reasonable to expect that chord-integrated densities will be measured exceeding the order of $1 \cdot 10^{21}$ $[m^{-2}]$. Therefore, the conversion factor of $5.61 \cdot 10^{20}$ in Equation 3.16 predicts that multiple fringe jumps will occur in the positive direction as density increases towards a peak magnitude, and then the same amount should occur in the negative direction as the plasma dissipates

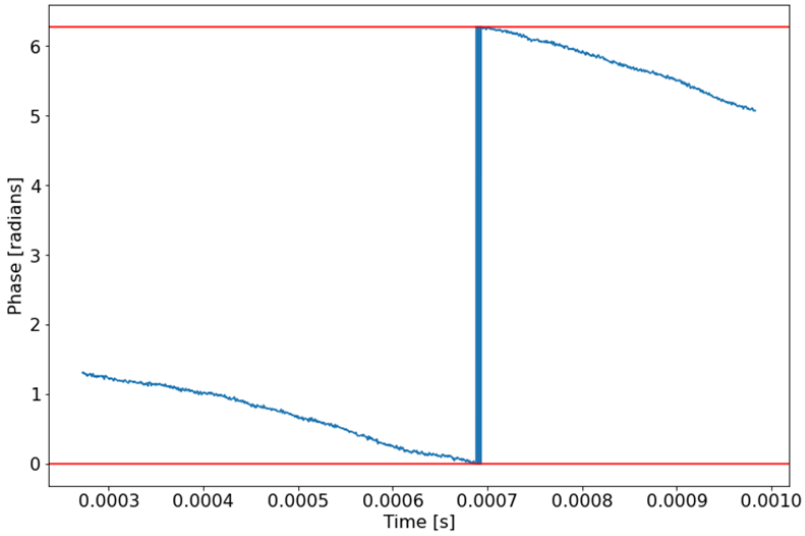

Figure 3.8: Example plot showing a fringe jump from 0 to 2π in a time-curve of the phase shift $\Delta\phi(t)$ due to ambient laboratory vibrations.

and the density curve returns to zero.

Two sources of fringe jumps, mechanical vibrations and observed plasma densities, have now been identified. Fringe jumps due to just these two sources are relatively simple to subtract in post-processing. However, electrostatic noise presents a third source of fringe jumps. If one time-point of phase shift data occurs close to the 2π boundary condition, then noise in the analog electronics could potentially push that data point past the fringe jump boundary. This behavior is why the Lissajous figure radius is maximized during beam alignment, as stated in Section 3.4.3. Electrostatic noise in the system is roughly constant with respect to Lissajous radius, therefore the Lissajous radius can be viewed as a metric to define the SNR (Signal to Noise Ratio) of an interferometer chord. This is why the small, fuzzy Lissajous in Figure 3.3 was labeled as representing a poorly-aligned chord, and the larger, sharper Lissajous was labeled as representing a properly-aligned chord. This behavior of fringe jumps due to electrostatic noise is more explicitly visualized in Figure 3.9.

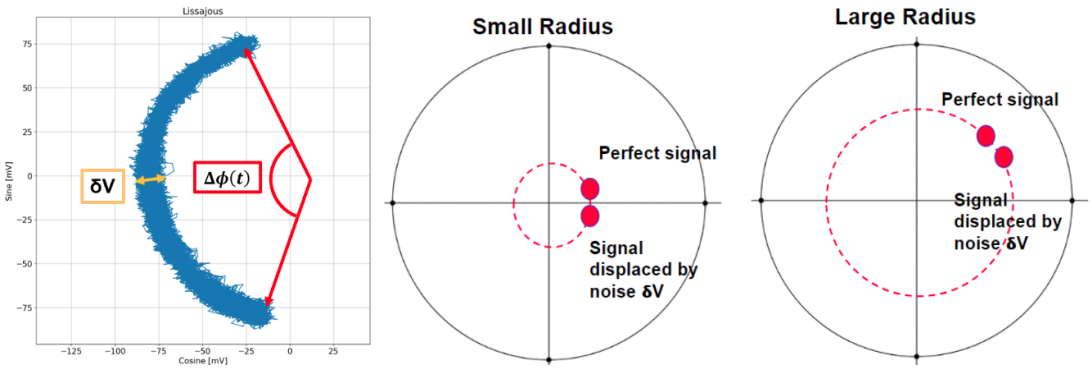

Figure 3.9: Left: plot of a vibrational Lissajous tracing a phase shift of $\Delta\phi(t)$ with an arc thickness δV due to electrostatic noise. Middle: graphical representation of how a small Lissajous radius could result in noise δV causing fringe jumps. Right: graphical representation of how a larger Lissajous radius is more robust against fringe jumps at the same magnitude of electrostatic noise.

All fringe jumps must be corrected in post-processing. Some of the fringe jumps can be caught in an automated manner using a continuous arctangent unwrapping function, which detects discontinuities above a certain threshold between adjacent data points and applies a correction of $\pm 2\pi$. However, it is typical for this automated subtraction to miss one or more fringe jumps, which will need to be subtracted manually. These manual corrections are performed by plotting the phase with respect to index, with vertical lines at each index where a discontinuity was detected above a certain threshold (which is lower than the correction threshold for the automated function). An example of such a plot is given in Figure 3.10.

3.6.3 Vibration Subtraction

As shown in Figures 3.8 and 3.3, ambient mechanical vibrations in the laboratory produce a contribution to the observed phase shift $\Delta\phi(t)$ which must be subtracted in post-processing. A closer look at the Lissajous figure given in Figure 3.9 is shown in Figure 3.11 as an ex-

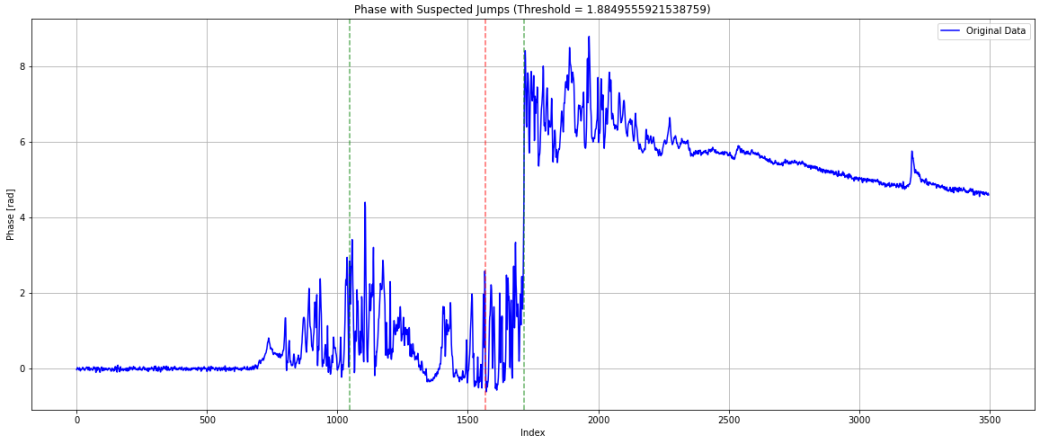

Figure 3.10: Plot of measured phase $\Delta\phi(t)$

plotted with respect to index with detected discontinuities marked with dashed vertical lines. A false detection of a positive fringe jump is seen slightly past index 1000. A false detection of a negative fringe jump is seen slightly past index 1500. A correct detection of a positive fringe jump is seen approximately at index 1700. For manual corrections on this set of data, the first two detections would be ignored, and the third would have a correction of -2π subtracted from all following indices.

ample of a recorded $\Delta\phi(t)$ signal immediately before plasma is measured.

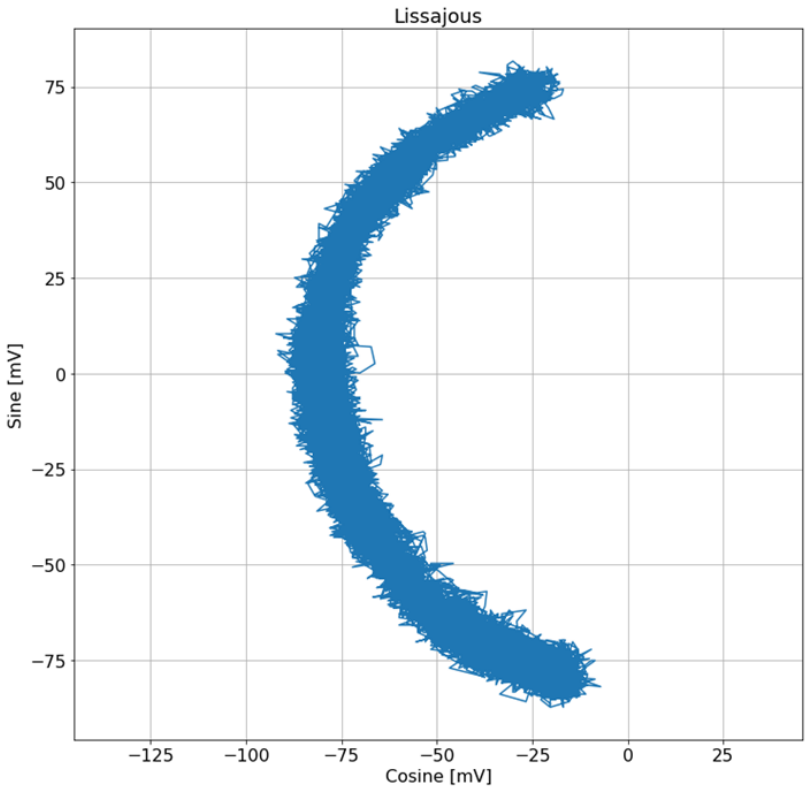

Figure 3.11: Lissajous figure produced by ambient vibrations collected over approximately 320 μs immediately before plasma is observed. This figure shows roughly 120° of vibrational contributions to $\Delta\phi(t)$, meaning that vibrations imposed approximately 0.4° per microsecond on the phase measured during this pulse.

The vibrational contributions to $\Delta\phi(t)$ can be viewed as linear in time for an initial automated subtraction of vibration signals in post-processing. A linear fit is applied to the $\Delta\phi(t)$ sampled before the first capacitor bank is triggered, and the fit is subtracting from the data collected over the duration of the pulse. This initial subtraction is depicted by a before and after plot in Figure 3.12.

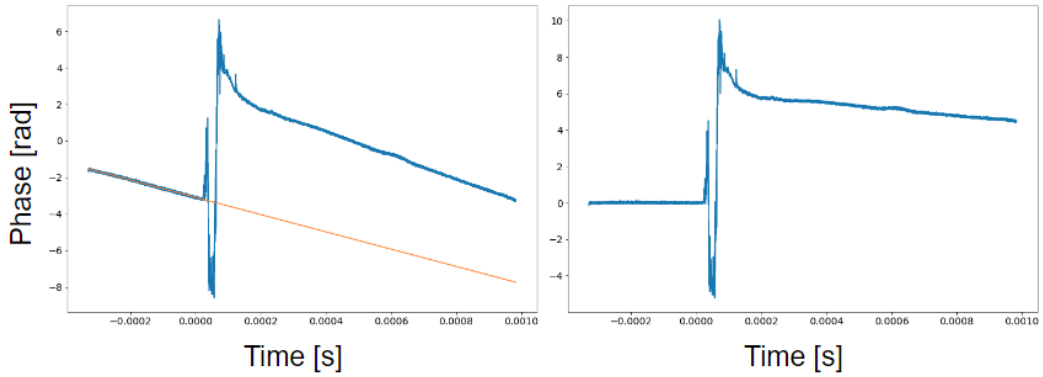

Figure 3.12: Before and after example plots of the initial linear fit for subtraction of vibrational contributions to $\Delta\phi(t)$.

Here it is important to note the order of operations for post-processing, and where the plots shown thus far fit into that order. First, the circular center offset is applied. Second, the initial automated fringe jump correction is applied. Third, the initial linear vibrational subtraction is applied, as depicted in Figure 3.12. Fourth, the manual correction of remaining fringe jumps is conducted as depicted in Figure 3.10. The final step towards achieving a continuous curve for $\Delta\phi(t)$ is one last vibrational subtraction step to account for the nonlinear vibrational behaviors imposed on the ZaP-HD rectangular windows during a pulse. The need for this additional correction is made apparent in Figure 3.13, which depicts the phase shift $\Delta\phi(t)$ after applying the manual correction shown in Figure 3.10.

The final corrections to the phase depicted in Figure 3.13 involve subtracting an additional linear fit to shift the full duration of plasma density measurements above zero. However, using another linear fit to account for nonlinear behaviors introduces uncertainty. To quantify this uncertainty, two linear fits are established. The first fit assumes that the entire reported duration of $\Delta\phi(t)$ must provide a plasma density greater than zero. The second fit uses the plasma current as measured by Rogowski coils to determine a boundary for a more conservative correction. With plasma present, the ZaP-HD device forms one large underdamped RLC circuit, therefore there is a point in the pulse at which the current

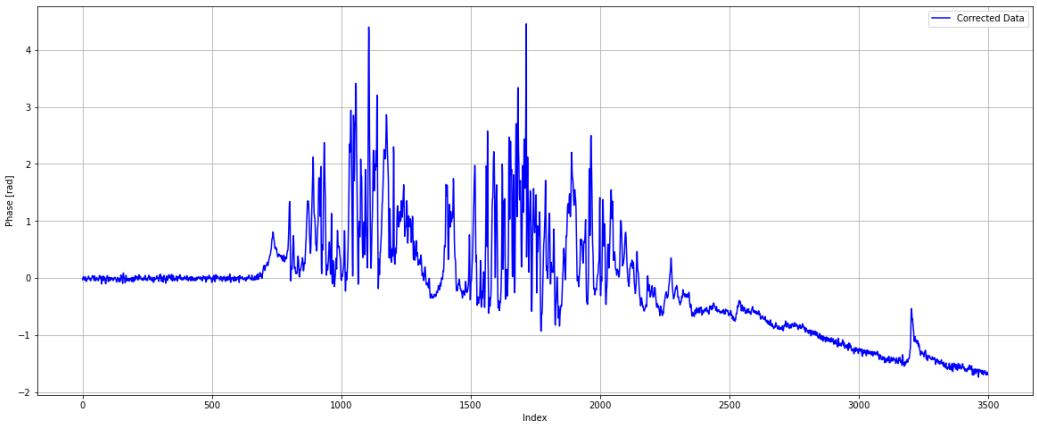

Figure 3.13: Example plot of $\Delta\phi(t)$ after applying the manual fringe jump correction. It can be seen that the total contribution of ambient vibrations has not been completely subtracted, as the phase gradually drops into the negatives over the course of the pulse. This would correspond to a negative plasma density, which is nonphysical.

through the plasma reverses direction, which shows up as the plasma current switching from positive to negative in the Rogowski measurement. The more conservative correction assumes that any data beyond this reversal of current can be disregarded as nonphysical, and only corrects for instances of zero density before the current reversal. Figure 3.14 shows these fits as calculated for the example trace in Figure 3.13.

The full-duration linear fit is subtracted from the curve of $\Delta\phi(t)$, and the resulting uncertainty is determined to be equal to the difference between the full-duration fit and the conservative fit. An example of the reported phase plotted with uncertainty bounds is given in Figure 3.15.

This concludes the post-processing corrections to the recorded time curve of phase shift $\Delta\phi(t)$. The final step to determine chord integrated density is to plug this curve into Equation 3.16.

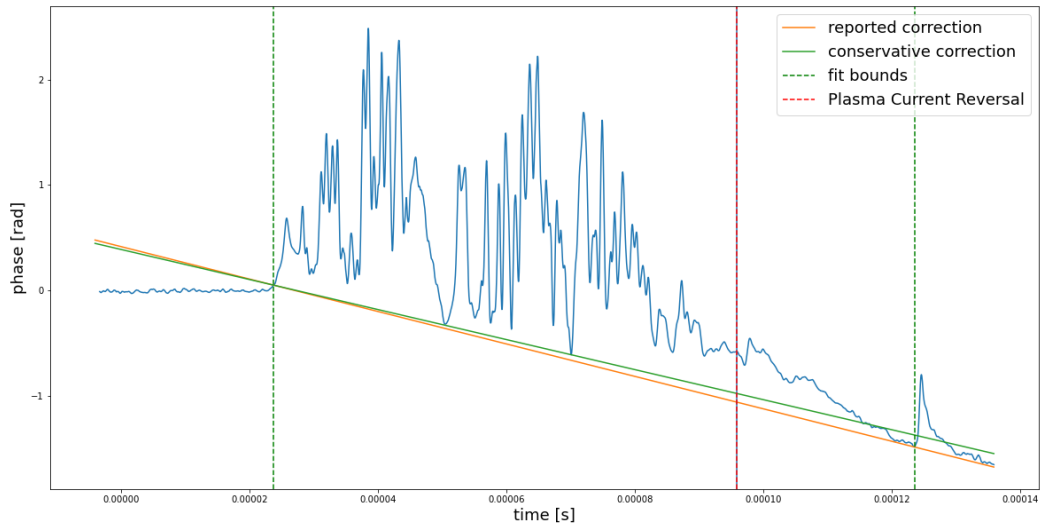

Figure 3.14: Plot of $\Delta\phi(t)$ after manual fringe jump corrections, with the two linear fits shown for the approximate subtraction of nonlinear vibrations. The bounds of the reported subtraction are marked by vertical green dashed lines. The end bound for the conservative subtraction is marked by a red vertical dashed line. The conservative linear fit is shown in orange, and the reported fit is shown in green.

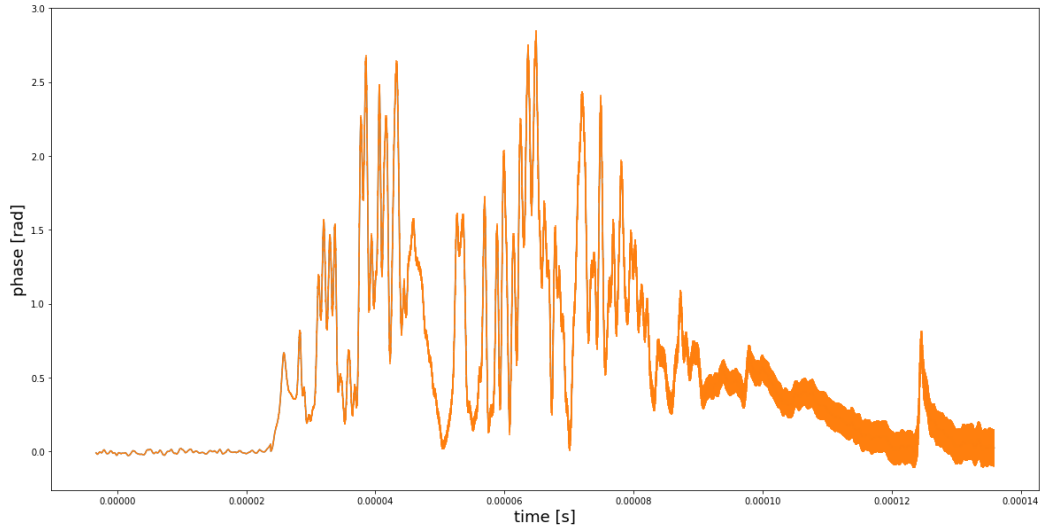

Figure 3.15: Plot of the example curve of $\Delta\phi(t)$ with the final vibration subtraction applied, and the resulting uncertainty bounds indicated.

3.7 Operation with Unequal Path Lengths

The classical understanding of interferometry as a tool demands that the paths followed by the scene and reference beams must be as close to equal in length as possible, and this rule has been closely followed by many experimentalists [27, 29, 30]. This is due to the assumption that path length differences increasing beyond the coherence length of a laser will result in a loss of the interference signal between the scene and reference beams, and thus rapid decay of SNR towards zero. Recent experiments, however, have shown that HeNe laser interferometers can exhibit SNR behavior which is spatially periodic with respect to path length difference ΔL [31, 32, 2]. The ZaP-HD interferometer was used to conduct a benchtop test of this behavior. A chord was aligned at increasing values of ΔL, with the radius of the resulting Lissajous figure recorded for each length difference increment. The results of this benchtop test were published by a ZaP-HD undergraduate student, and are plotted in Figure 3.16 [2].

Figure 3.16 shows that a Lissajous radius of nearly 200 millivolts was achieved at $\Delta L = 0\ m$ and $\Delta L = 1.5\ m$. The coherence length of the HeNe laser used on ZaP-HD is on the order of 20 centimeters, so this proves that a favorable SNR can be achieved for ΔL values many times greater than the laser coherence length. It is noted that this curve does not follow a uniformly periodic behavior, as previous experiments might suggest [32, 31]. Referenced experiments used homodyne Michelson interferometers with motorized autostagers to collect data at many values of ΔL without introducing variability between data points due to aligning beams by hand. These experienced resulted in distinctly sinusoidal envelopes of interference. This benchtop experiment, conducted with a Mach-Zehnder heterodyne quadrature interferometer, was conducted at a coarser spatial resolution by aligning lasers by hand for each observed ΔL data point, which is a likely explanation for the shape of the curve. Regardless of whether the behavior is a proper sinusoid, this data does show that the ZaP-HD interferometer can be useful at path length differences exceeding one meter.

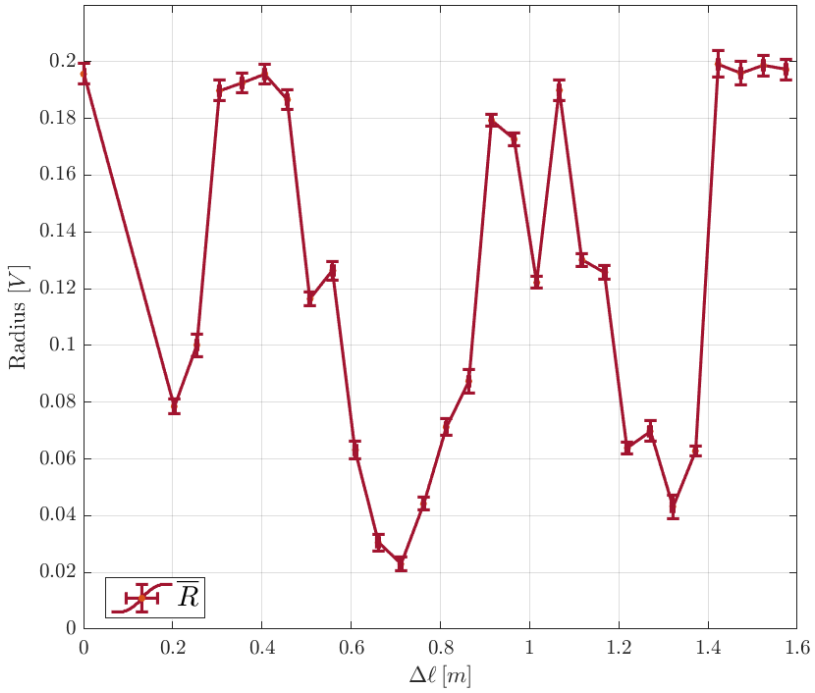

Figure 3.16: Plot of Lissajous radii formed by ZaP-HD interferometer chords aligned with increasing path length differences between the scene and reference beams [2]. Note that the same radius is reported for $\Delta L = 0\ m$ and $\Delta L = 1.5\ m$.

3.7.1 Motivation for Unequal Path Operation

The HeNe interferometer shares relatively small windows with many optical diagnostics on ZaP-HD. Clear optical paths are required to measure flow velocity, plasma temperature, electron density, impurity concentrations, and electrode surface temperatures, and to record high speed video. Electron density alone does not provide the full story of what is happening inside the ZaP-HD device, a well-diagnosed plasma will have measurements of multiple plasma parameters taken at the same location at the same time. This creates a demand for flexibility of optical configurations. For example, plasma temperatures are measured by Doppler broadening spectroscopy using light collected from the radial telescope. It can be seen in Figure 3.17 that the radial telescope is mounted on top of ZaP-HD such that it would block the paths of HeNe interferometer reference beams in the typical Mach-Zehnder configuration as shown in Figure 3.4. Therefore, to simultaneously measure electron densities and ion temperatures at the same location in ZaP-HD, the HeNe interferometer requires the flexibility to operate outside of the typical Mach-Zehnder configuration.

Additionally, the spatial resolution of the HeNe interferometer is limited by how tightly parallel scene beams can be grouped in passing through ZaP-HD. The smallest mirrors available in the laboratory are 1 inch in diameter, so achieving beam spacings smaller than 1 inch without beam clipping often requires the flexibility for creative alignment configurations.

To summarize the motivation for pursuing alternative alignment configurations, it is generally favorable for the HeNe interferometer to not be restricted to one rigid anatomy. Two different types of unequal path setup were explored for this thesis in the pursuit of this desired flexibility. Both setups keep the reference beam confined to the optical breadboard where the laser and Bragg cell are mounted, with only the scene beam leaving this breadboard to probe the plasma and return for recombination.

Figure 3.17: Photograph of the radial telescope mounted atop ZaP-HD. It is clear that if the HeNe interferometer is restricted to the typical Mach-Zehnder configuration, that this telescope will block the reference beams. This prevents time-resolved measurements of electron density and ion temperature from being collected in the same location simultaneously.

3.7.2 Unequal Path Single-Pass

The first unequal path setup is referred to as the single-pass configuration, because it involves the scene beam passing through the ZaP-HD experiment once, and then returning over the experiment to be recombined. A diagram of one single-pass chord is given in Figure 3.18.

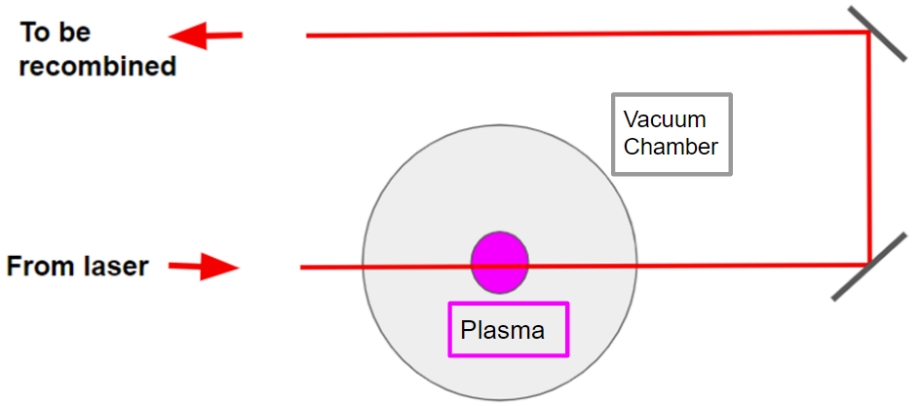

Figure 3.18: Diagram of the scene beam path to and from the plasma for one single-pass chord. View is of a circular 2-D cross-section at some arbitrary axial location. The scene beam passes through the plasma, and is returned by passing over the top of the vacuum chamber as directed by two turning mirrors.

3.7.3 Unequal Path Double-Pass

The second unequal path setup is referred to as the double-pass configuration, because it involves the scene beam passing through the ZaP-HD experiment and then returning by retracing its own path back through the device on the second pass. A diagram of one double-pass chord is given in Figure 3.19.

Figure 3.19 shows the scene beam passing through a planar beam splitter before making a first pass through the plasma, and then reflecting off the same beam splitter to be recom-

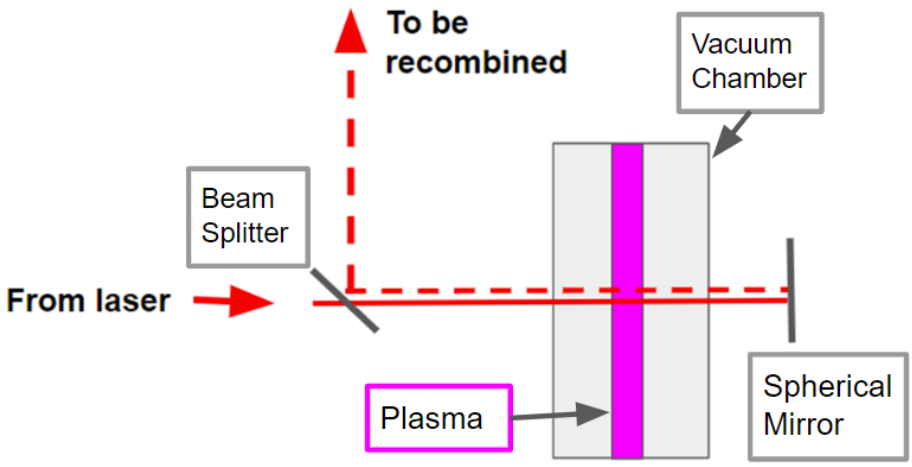

Figure 3.19: Diagram of the scene beam path through the plasma for one double-pass chord. View is from above the ZaP-HD device. The scene beam passes through the plasma, and then returns retracing its own path. A collinear return path is made possible by the planar beam splitter.

bined after returning from the second pass. This beam splitter is required for a collinear return path, but results in approximately 75% attenuation of the scene beam power. In an attempt to compensate for this attenuation, the scene beam is returned by a concave spherical mirror with a 2 m radius of curvature, chosen to be on the order of the path length difference ΔL to counteract the divergence of the scene beam by focusing its spot size to a smaller diameter [32]. Since the scene beam passes through the plasma twice, the conversion factor used in Equation 3.16 must be divided by two, yielding Equation 3.21.

$$N_e = \frac{5.61 \cdot 10^{20}}{2}(\Delta\phi(t)) \tag{3.21}$$

Chapter 4

EXPERIMENTAL MEASUREMENTS

This chapter presents data from selected ZaP-HD pulses. Data from each pulse is denoted by a "shot number" in the format "YYMMDD###" such that, for example, shot number 250424020 would refer to the 20th pulse taken on April 24th of 2025. When viewing plots of time-resolved data, time "$t = 0$" refers to the instant at which the acceleration bank was triggered. Negative timestamps are before the acceleration trigger, and positive timestamps are after. For all pulses presented here, it should be assumed that the time "$t = \tau_D = 20\ \mu s$" will be the instant at which the compression bank was triggered, unless explicitly stated otherwise.

4.1 Preliminary Experimental Campaign

Measurements recorded during a previous science campaign conducted on ZaP-HD contribute to the motivation for this thesis investigation. The HeNe interferometer was used to survey average pinch densities at four evenly spaced locations along the center axis of the ZaP-HD experiment [33]. A diagram of this measurement configuration is given in Figure 4.1. These measurements were recorded using the typical Mach-Zehnder configuration depicted in Figure 3.4 with equal scene and reference beam path lengths.

Two plots of average densities recorded using this configuration are given in Figure 4.2. Significant drops in density are observed between 20 and 30 centimeters downstream of the end of the middle electrode.

High speed video taken using the Kirana camera during this previous science campaign revealed an extremely sudden dropoff in visible emissions in the region 20 to 30 centimeters

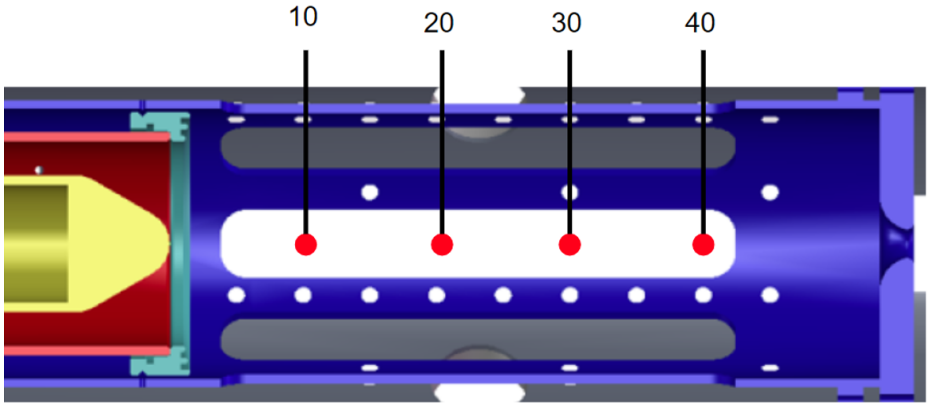

Figure 4.1: ZaP-HD assembly region diagram showing HeNe interferometer chord locations for the course axial survey conducted during a previous science campaign. Chord locations given in centimeters downstream from the end of the middle electrode (red).

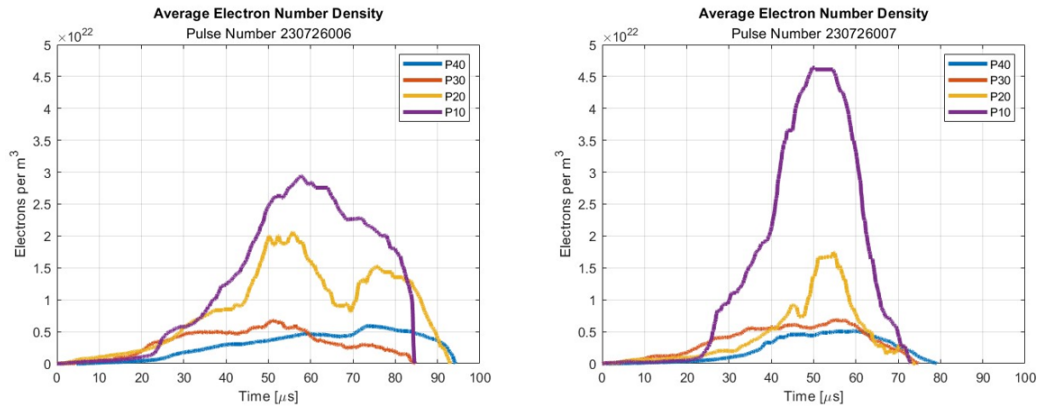

Figure 4.2: Average electron density plots recorded during the previous science campaign for an axial density survey. Plot legend labels indicate distance downstream (in centimeters) from the end of the middle electrode. Notable density drops are observed between 20 and 30 centimeters.

downstream of the middle electrode end in ZaP-HD. A frame from one of such videos is given in Figure 4.3.

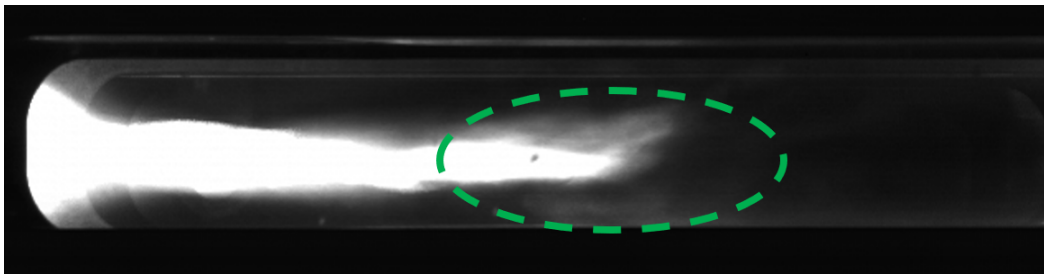

Figure 4.3: Still frame from a high-speed video of ZaP-HD assembly region. Green dashed oval roughly encloses the region 20-30 centimeters downstream of the end of the middle electrode. An immediate dropoff in visible plasma emissions is noticed within this region.

Observations made during this previous experimental campaign revealed electron density and plasma emissions drastically decreasing in the ZaP-HD assembly region between 20 and 30 centimeters downstream of the end of the middle electrode. These observations motivated closer investigation of this region for this thesis.

4.2 Note on ZaP-HD Configuration Changes

With these experimental results, it is important to note that the physical configuration of ZaP-HD has been changed in two notable ways since the previous experimental campaign described in Section 4.1. The first is the configuration of the vacuum vessel. During the previous campaign, ZaP-HD had a 1-meter long vacuum chamber extension such that there was approximately 120 cm of distance for unobstructed exhaust plume expansion beyond the end wall of the outer electrode before reaching the vacuum chamber boundary. That extension was removed before this campaign, meaning a gap of only 20 cm downstream of the endwall. This reduction in vacuum chamber volume has resulted in typical gas puff injections (10's of milligrams of H_2) providing higher total pressure readings than before.

This change is not expected to impact the results of this study significantly, as this study does not measure the expansion of the exhaust plume, and the timescale of a ZaP-HD pulse is faster than the timescale of a gas puff expanding to fill the entire chamber volume.

The second change, which could reasonably impact the results of this study to a significant degree, is the position of the inner electrode. This study is conducted concurrently with a PMI (plasma material interaction) study on the ZaP-HD nosecone. This PMI study requires direct optical paths to the nosecone for multiple instruments, so the inner electrode has been shifted inward to enable such viewing paths through the assembly region rectangular windows. This displacement of the inner electrode results in the tip of the nosecone protruding roughly 8 cm into the assembly region. A diagram depicting this change is given in Figure 4.4.

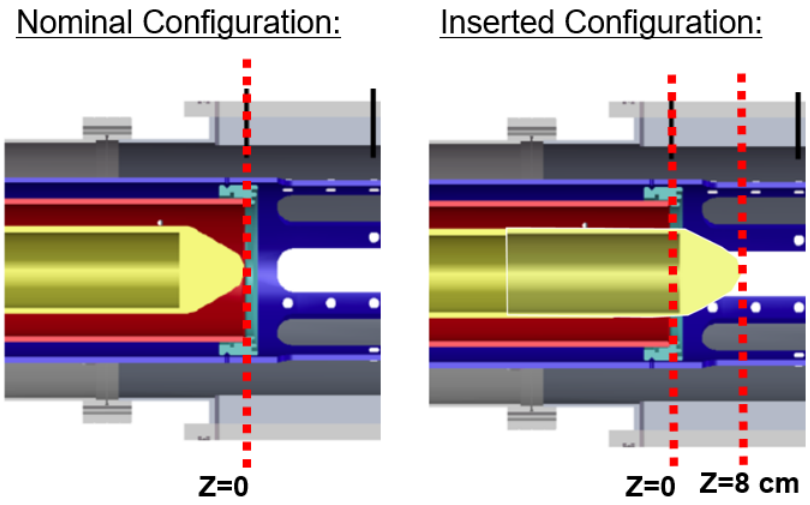

Figure 4.4: Left: Diagram of nominal ZaP-HD electrode configuration, with the nosecone tip flush with the end of the middle electrode. Right: Diagram of inserted ZaP-HD electrode configuration, with the nosecone displaced 8 centimeters downstream of the end of the middle electrode.

It is undeniable that this changes the functionality of ZaP-HD. As previously shown in

Figures 2.1 and 2.2, the ZaP-HD acceleration region was designed for the tip of the nosecone to be flush with the end of the middle electrode. This design was chosen so that the current sheet would curve inward towards the machine center axis to form a collimated plasma jet in the assembly region before the triggering of the compression bank. With the nosecone now protruding 8 cm beyond the originally designed end of the accelerator, it is likely that the initial current sheet will experience an outward acceleration as it enters the assembly region. This has the potential to significantly alter the behavior of the plasma during the transition between acceleration and compression, as the geometry guiding the "snowplow" has changed. An illustration of the possible current sheet modification is given in Figure 4.5.

With this significant change to the function of the accelerator, it is noted that the experimental findings of this thesis may not lead to confident conclusions which are relevant to the nominal operation of ZaP-HD.

4.3 Axial Density Measurements

This section presents data collected using the interferometer in a similar measurement configuration to what is shown from the previous campaign in Figure 4.1, but with a tighter spacing of chords aligned with the ZaP-HD center axis. The furthest upstream chord is located 21 centimeters downstream of the end of the middle electrode, with an interchord spacing of $2\frac{1}{3}$ cm for the three following chords. Therefore, there are chords placed 21 cm, 23.3 cm, 25.6 cm, and 28 cm downstream of the end of the middle electrode. A diagram of this configuration is given in Figure 4.6.

Figure 4.7 shows a time-resolved plot of chord integrated electron densities recorded using the measurement configuration shown in Figure 4.6 for shot number 250424020[1]. The first items to note on this plot are a few sanity checks to confirm that the data appears

[1]Shot 250424020 is chosen as a representative dataset for demonstration purposes in this chapter. This is because shot 250424020 required the lowest magnitude of manual discretionary interventions in post-processing (as described in Section 3.6) to pass all "sanity checks" for verifying confidence in interferometer data. Between all four chords combined, less than 10 manual fringe jump corrections were needed.

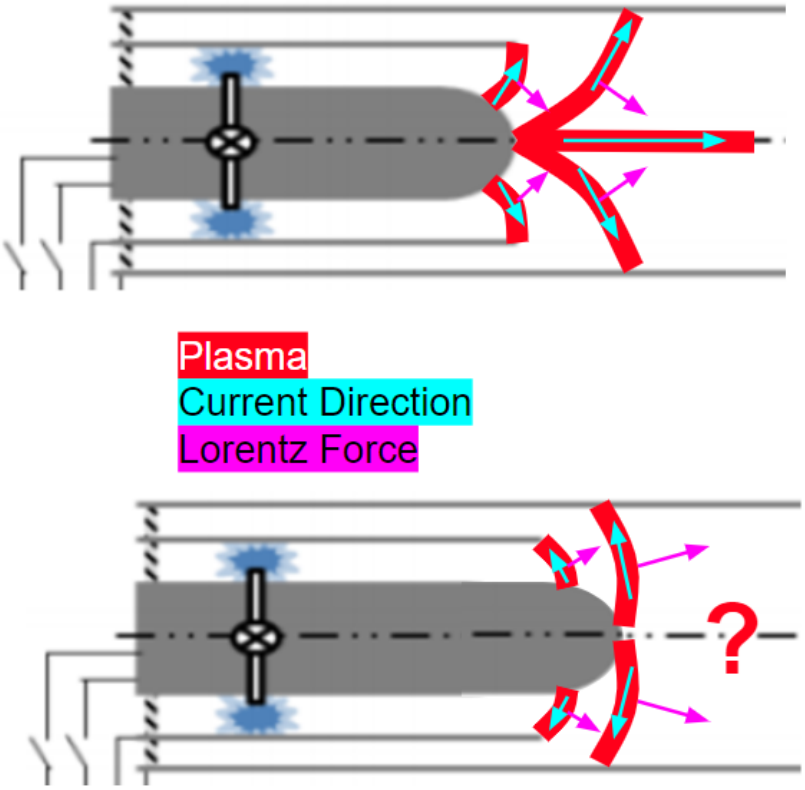

Figure 4.5: Top: depiction of nominal snowplow, with Lorentz force encourage the current sheet to collapse onto the center axis of the ZaP-HD device. Bottom: depiction of a possible consequence to the electrode displacement, Lorentz force accelerates current sheet outwards as it exits the acceleration region, unknown effects downstream.

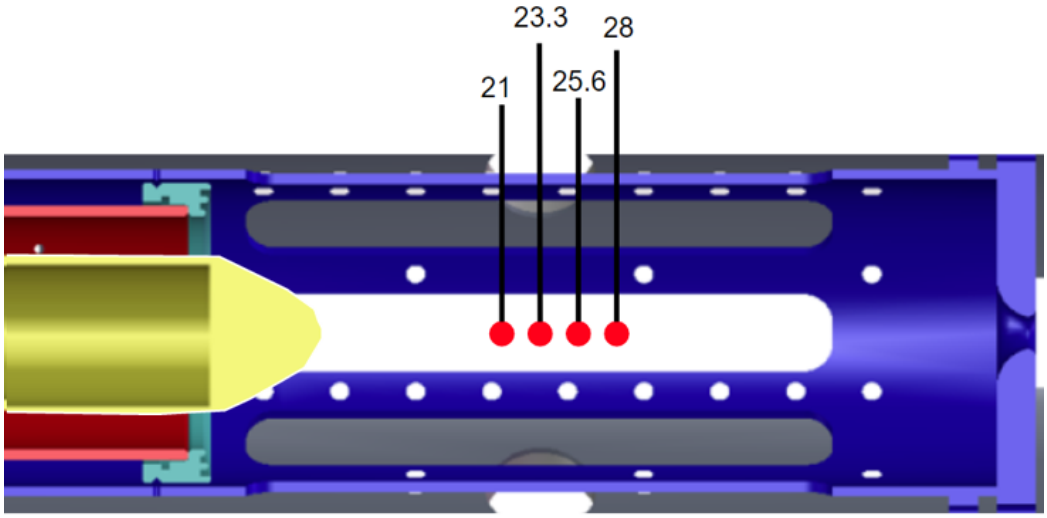

Figure 4.6: ZaP-HD assembly region diagram showing HeNe interferometer chord locations for the fine-spaced axial survey configuration between 21 and 28 centimeters. Chord locations given in centimeters downstream from the end of the middle electrode (red).

physically valid. The first is that the density equals approximately zero leading up to the acceleration discharge trigger at $t = 0\ \mu s$. The second is that a steep rise in density is observed after the compression discharge trigger at $t = 20\ \mu s$. The third is that the density returns to approximately zero within the expected pinch timescale. In Figure 4.7, this return to zero is shown at approximately $t = 120\ \mu s$, which is within a reasonable range of 80 μs to 140 μs [34], [35].

One additional check to verify that the data appears reasonable involves taking a closer look at the initial rise in density immediately after the compression trigger, as shown in Figure 4.8. The order in time at which the peaks appear initially is observed to indicate upstream chords seeing bulk plasma before downstream chords. This observation leads to the use of the interferometer as a time-of-flight probe, by dividing the distance between chords by the time between their respective density peaks to verify that the result is comparable to expected initial bulk-flow velocities. The anticipated range is between 60 and 140 kilometers per second, as determined by previous experiments using ion-doppler spectroscopy [36, 1].

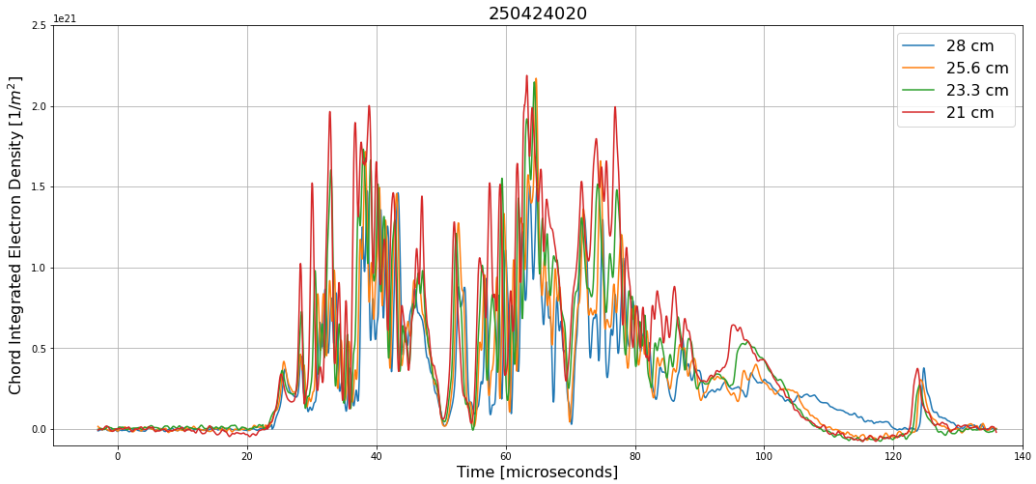

Figure 4.7: Chord-integrated density traces from shot 250424020. The time spans from several microseconds before the acceleration trigger to after all plasma is assumed to have dissipated. A rise in all signals is observed shortly after the compression bank trigger at $t = 20\ \mu s$. All signals show rapid, large-amplitude oscillations between the initial rise and approximately $t = 80\ \mu s$. All signals reach zero density at approximately $t = 120\ \mu s$, followed by one last noticeable spike before quickly returning to zero density.

The initial velocity for pulse 250424020 is calculated at 103 kilometers per second, which is right in the middle of the anticipated range.

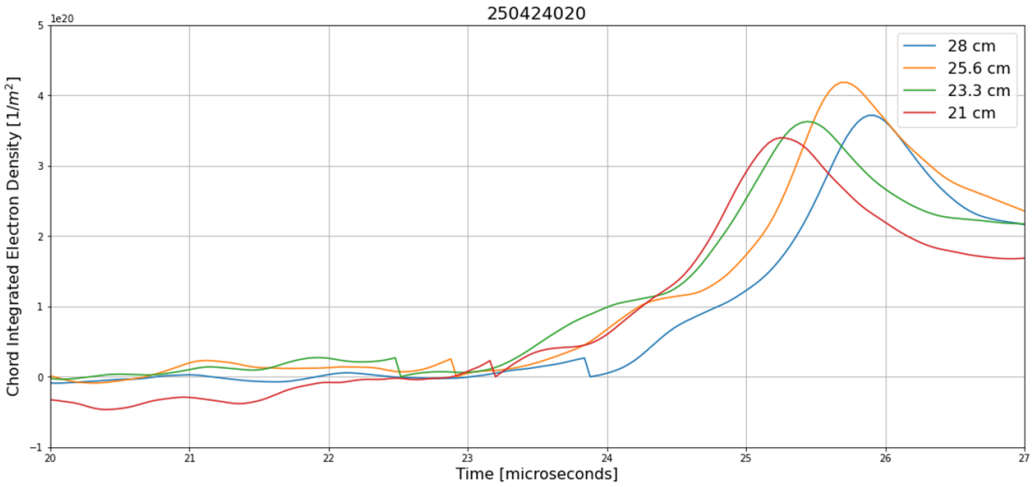

Figure 4.8: Plot of density traces from pulse 250424020 showing a time range of 20 μs to 27 μs. It is seen that the order at which density peaks above the noise level are first measured chronologically matches up with the order of the chord locations in the streamwise direction. This corresponds to the data passing the sanity check for ensuring that plasma is observed to move in the expected direction.

The density traces for shot 250424020 as shown in Figure 4.7 indicate rapid oscillations in density. If the pinch is collinear with the center axis of the machine, then this would imply high-frequency longitudinal density perturbations. This disagrees with theoretical predictions of linear density behavior. The linear density of a Z-pinch is defined in Equation 4.1, where a is the characteristic pinch radius. This linear density is the measure of particles per unit length along the pinch axis. According to magnetohydrodynamic theory, linear density is expected to remain constant along the length of the pinch [37].

$$N_{linear} = \int_0^a n_e(r) 2\pi r dr \tag{4.1}$$

While this investigation is based on observations of ZaP-HD linear density decreasing as the plasma flows downstream, the anticipated drop in density observed in the preliminary campaign occurs monotonically over a much longer timescale, rather than oscillating rapidly on a 1-2 microsecond timescale.

High speed video footage recorded by the kirana camera offers insight into what is actually causing these rapidly oscillating density measurements. Two frames taken 500 nanoseconds apart from each other are shown in Figure 4.9. Distance scaling in these frames is determined using the known size of the visible bolt hole on the nosecone tip to determine a pixels-per-millimeter scaling. These two frames show the centroid of visible emissions traversing a vertical distance of approximately 25 mm at the measurement location 21 cm downstream of the middle electrode. The incident diameter of the scene beam at the ZaP-HD windows is approximately 3 mm. Therefore, Figure 4.9 suggests that the pinch centroid is capable of traversing a distance greater than 8 times the diameter of a HeNe chord within a span of half a microsecond.

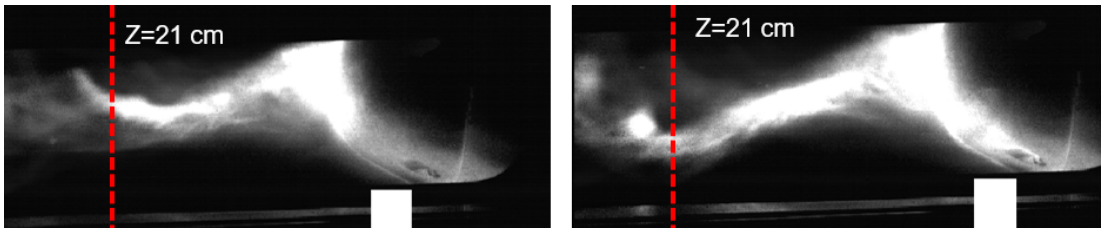

Figure 4.9: Two adjacent high-speed video frames recorded 500 nanoseconds apart. The location 21 centimeters downstream of the middle electrode is shown by the red dashed lines. It can be seen that the pinch moves a considerable vertical distance at this location between frames.

Figure 4.9 shows that the pinch can experience radial displacements many times larger than the diameter of a HeNe chord in a short timespan. Kirana videos from dozens of other pulses in the inserted electrode configuration show similar short-timescale radial displace-

ments in ZaP-HD plasmas. This leads to the assumption that the rapid perturbations to measured density shown in Figure 4.7 are not actually longitudinal density perturbations along the pinch axis, but are due to the pinch wandering back and forth across the interferometer chords. Each observed peak likely corresponds to the time at which the pinch centroid intersected the scene beam of the chord in question. Therefore, to characterize the behavior of the average electron density in the pinch as the plasma flows downstream in time, data from clearly defined peaks is analyzed to minimize uncertainty due to ambiguities in the plasma geometry. For this analysis, which is discussed in detail in Cahpter 5, six total pulses are considered. These pulses are taken with acceleration discharges of 9 kilovolts and compression discharges of 8 kilovolts. Chord-integrated density plots for these pulses are provided in Figure 4.16.

Several immediate observations are noted for the data presented in Figure 4.16. All of this data was collected on the same day, April 24th of 2025. From this data, pulses 008, 009, 010, and 019 each provide one density peak which is identified as an outlier. These outliers are defined as a local maxima on one chord which exceeds 150% of the maximum magnitude measured on any of the other 3 chords within a time window of $\pm 3\mu s$ of the peak in question. There is not sufficient confidence to dismiss these outliers as entirely non-physical, however, there is enough suspicion to omit these specific peaks from the analysis of axial density gradients. Additionally, it is noted that pulse 019 records a local minima at a negative density value shortly after $t = 60\ \mu s$ at the $z = 25.6\ cm$ location. This is obviously not a real physical measurement, and is most likely an artifact of errors in fringe jump removal. Due to the uncertainty introduced by this issue, denisty data collected after $t = 60\ \mu s$ for this pulse only is not included in the analysis of axial density gradients.

4.4 Magnetic Field Measurements

Analysis of axial density gradients is supported by data collected using the azimuthal arrays of magnetic field probes discussed in Section 2.2.3. The three 8-probe arrays located at $z = +15,\ 30$, and $45\ cm$ are used to corroborate interferometer data on average density

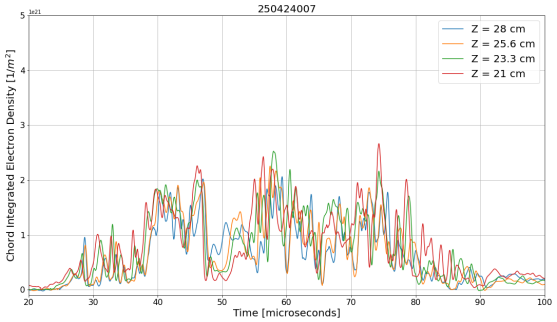

Figure 4.10: Pulse 250424007

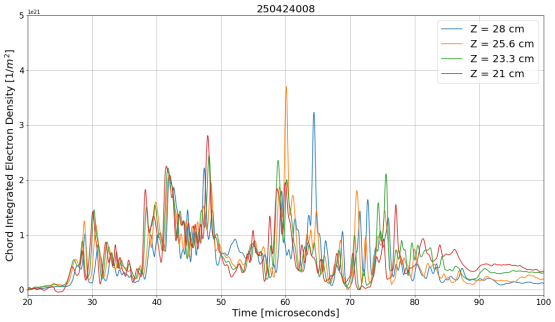

Figure 4.11: Pulse 250424008

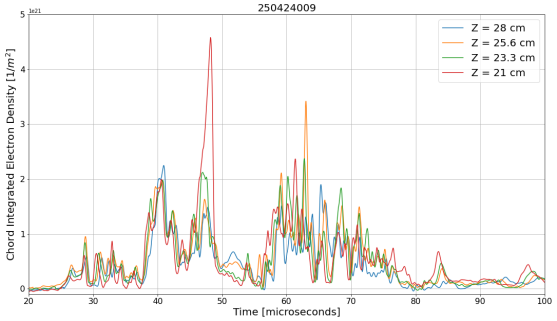

Figure 4.12: Pulse 250424009

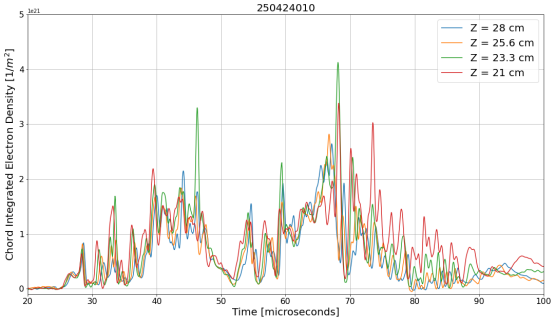

Figure 4.13: Pulse 250424010

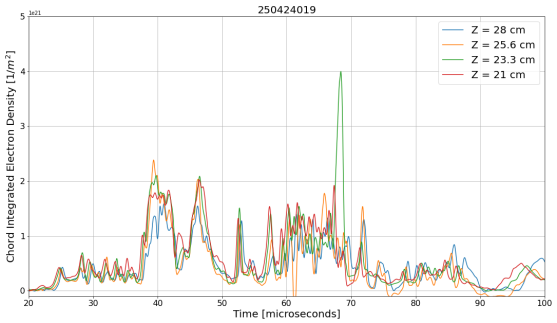

Figure 4.14: Pulse 250424019

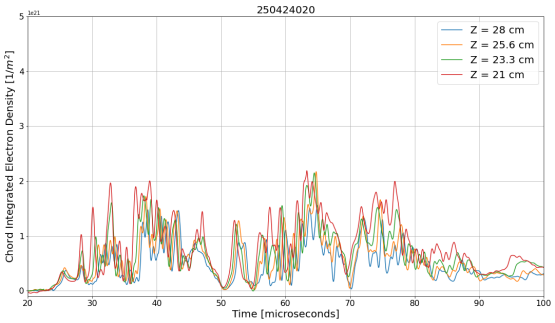

Figure 4.15: Pulse 250424020

Figure 4.16: Chord integrated density data for selected pulses taken with capacitor bank charges of 9 kV acceleration and 8 kV compression. Ranges shown are equal on all axes for ease of comparison. Time given from 20 to 100 μs, N_e vertical limit is $5 \cdot 10^{21}$ m^{-2}

.

behavior. for this purpose, data from 11 pulses is considered, all taken with compression discharge voltages of 8 kV and acceleration discharge voltages of 9 kV. Plots of the time-resolved magnetic field data from these three arrays during the example pulse of 250424020 are shown in Figure 4.17. Data from the 10 remaining pulses which are considered is presented in Appendix A.

From the magnetic field plots in Figure 4.17, the peak observed magnitudes are greater than 0.6 T at $z = +15$ cm, less than 0.4 T at $z = +30$ cm, and greater than 0.4 T at $z = +45$ cm. The peak magnetic field does not decrease monotonically as the plasma flows downstream, but increases between 30 and 45 centimeters. This is due to the accumulation of magnetic flux caused by stagnation of the plasma flow at the end wall. For the purposes of this thesis, analysis is conducted assuming that the effects of plasma stagnation do not back-propagate far enough upstream to be noticeable in measurements taken at $z \leq 30$ cm.

4.5 Radial Disturbance Measurements

This section presents data collected using an interferometer configuration with chords at two axial positions and two impact parameters, such that the incident beams form a rectangle with one side being collinear with the center axis of the ZaP-HD device. A diagram of this configuration is given in Figure 4.18. This setup is referred to as the "2+2" configuration. All measurements taken with this chord arrangement were using the double-pass unequal path length configuration.

Measurements taken with this configuration did not reliably produce density data which can be trusted. This is believed to be a result of flaws in the interferometer setup. This is discussed in detail in Chapter 5. Only one pulse produced HeNe interferometer data which can be confidently reported as physical on all four chords. The density data for this pulse, number 250508016, is shown in Figure 4.19.

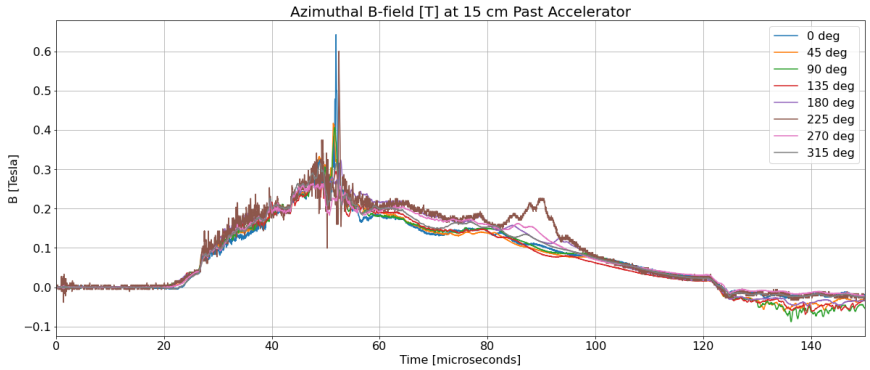

(a) Magnetic field data for $z = +15\ cm$.

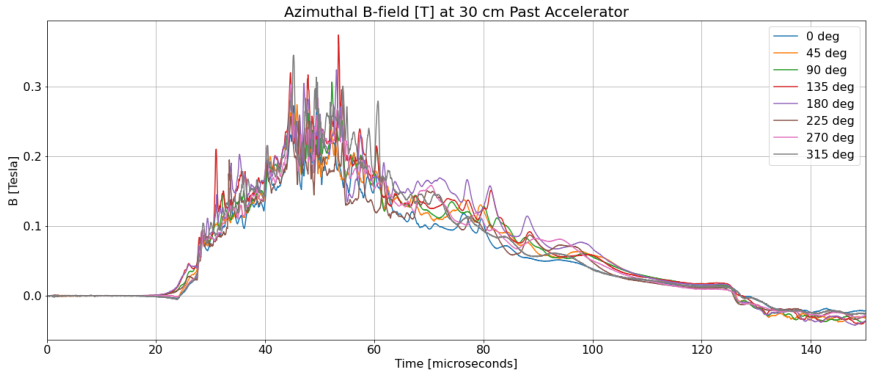

(b) Magnetic field data for $z = +30\ cm$.

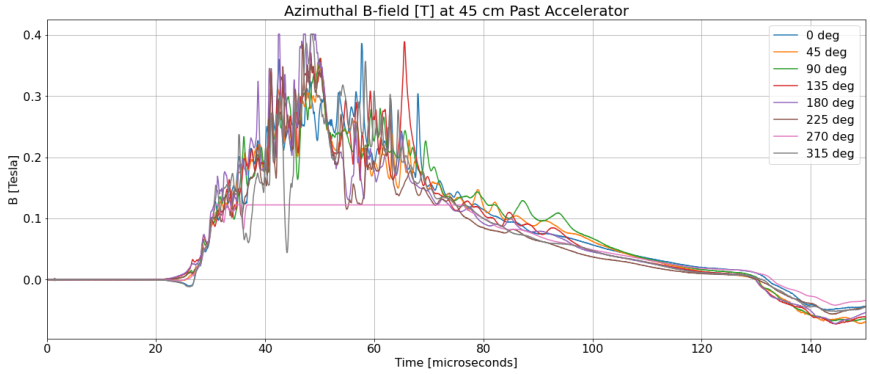

(c) Magnetic field data for $z = +45\ cm$.

Figure 4.17: Time-resolved magnetic field probe data for pulse 250424020. Time shown ranges from 0 to 150 μs.

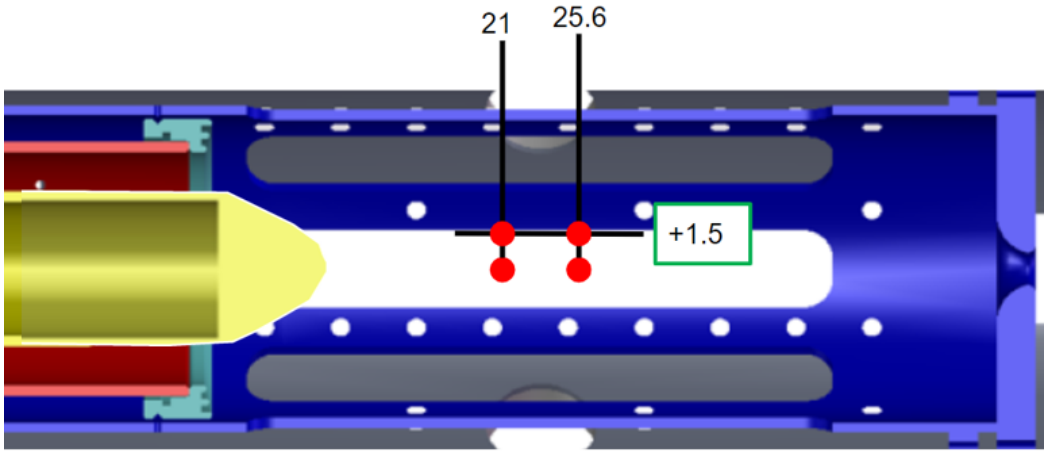

Figure 4.18: ZaP-HD assembly region diagram showing HeNe interferometer chord locations for the "2+2" configuration. Chord spacings downstream of the middle electrode end are indicated in centimeters above the figure. The green outlined box indicates two chords being placed at an impact parameter of 1.5 cm above the ZaP-HD center axis.

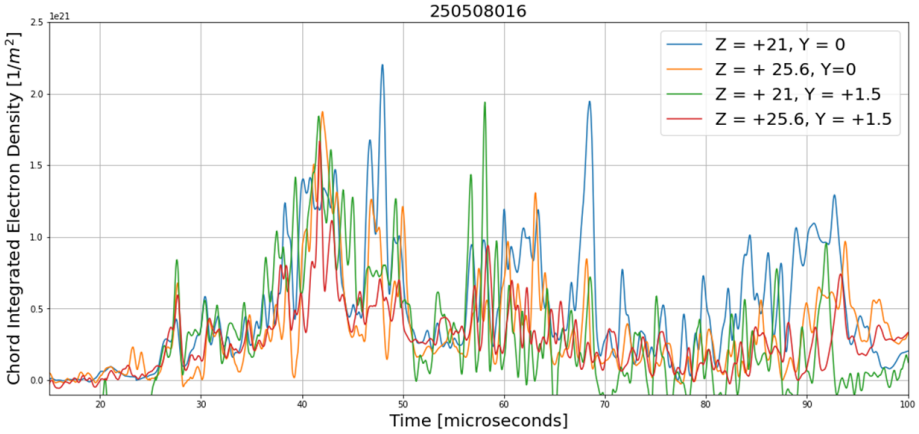

Figure 4.19: Density plot for pulse 250508016, taken using the 2+2 measurement configuration.

Chapter 5

ANALYSIS OF EXPERIMENTAL RESULTS

5.1 Axial Density Gradients

This thesis is concerned with plasma density behavior within the period during which stable heating and compression occurs, referred to as the quiescent period. The quiescent period is when fusion reactions are expected to occur due to the highest densities and temperatures being achieved within this time frame [38]. Experiments on the FuZE device have demonstrated that peak fusion reaction rates, as determined by time-resolved measurements of neutron emissions, closely correspond to peaks in observed plasma current in time [39]. Therefore, analysis for the density data introduced in Section 4.3 is limited to the time boundaries defined by the magnitude of the plasma current being measured as greater than 85% of the peak observed plasma current for each respective shot. For the six shots considered in this analysis, this window spans between $30 \pm 2\ \mu s$ and $63 \pm 2\ \mu s$.

Within the established time windows for each pulse, two sets of four clearly defined peaks between adjacent chords are selected for analysis. This is based on the assumption of density peaks corresponding to the pinch center intersecting the scene beam at the location of the measured peak. For the scope of this analysis, it is assumed that a set of four adjacent peaks in measured density which occur in chronological agreement with the direction of the plasma flow must correspond to a radial displacement which causes a discrete point of intersection of the pinch centroid with the machine center axis to move downstream with the bulk plasma flow. One example of a set of adjacent density peaks is given in Figure 5.1.

Once a set of four peaks is identified, the gradient slope is calculated for the three equal axial distances between the four HeNe interferometer chords. The gradient scale length over each of these distances is then calculated by multiplying the inverse of the gradient slope by the peak density measured at the upstream chord of the two chords spanning the interval

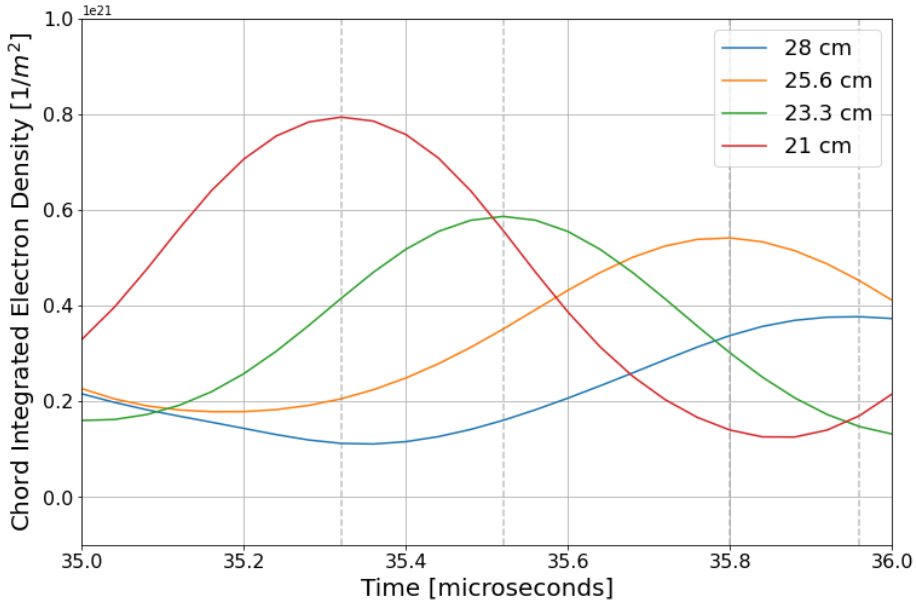

Figure 5.1: Example of an identified group of four clearly defined adjacent peaks in plasma density. Downstream peaks occur later than upstream peaks, as expected. Shown time span is $35 - 36$ μs for pulse 250424020.

in question, as shown in Equation 5.1. For example, this means that for the gradient scale length between $z = 21\ cm$ and $z = 23.3\ cm$, the inverse of the gradient slope between these two locations is multiplied by the peak density measured at $z = 21\ cm$.

$$L(z) = \frac{N_e(z)}{|\frac{dN_e}{dz}|} \tag{5.1}$$

This $L(z)$ value resulting from Equation 5.1 can be interpreted as the distance downstream from the location of measurement at which the plasma density would reach zero if the observed gradient slope continued linearly along the full length of the pinch, meaning a smaller value of $L(z)$ corresponds to a steeper rate of density decrease. For example, a calculated $L(z)$ of 20 cm for the measurement location of $z = 21\ cm$ would translate to the plasma density reaching zero at the location $z = 41\ cm$, which is $L = 20\ cm$ downstream of the measurement location. It is critical to note that the density gradient certainly does not actually follow a first order linear slope over a distance of 20 cm, and these values calculated for $L(z)$ simply offer a relative metric to compare the relative density decreases which occur over the three intervals between the four interferometer chords. Conducting this analysis over two groupings of adjacent peaks for six total pulses for a sample size of twelve, the average gradient scale lengths are determined for each interval, as given in Table 5.1.

Window	Mean $L(z)$ $[cm]$	Standard Deviation σ $[cm]$
$z = 21\ cm$ to $z = 23.3\ cm$	22.8	15.9
$z = 23.3\ cm$ to $z = 25.6\ cm$	31.7	50.0
$z = 25.6\ cm$ to $z = 28\ cm$	14.6	7.1

Table 5.1: Table showing the mean density gradient scale length $L(z)$ and corresponding standard deviation σ for each of the three distance intervals between interferometer chords.

It is seen in Table 5.1 that both the shortest density gradient and the smallest standard deviation occur in the most downstream interval of $2\frac{1}{3}\ cm$. This indicates that among the three measured intervals, the largest magnitude of density decrease, as well as the most

consistent density decrease behavior, occurs between $z = 25.6$ and $z = 28$ cm downstream of the end of the middle electrode. In addition to the gradient scale length analysis, the total percent drop in density observed between $Z = 21$ cm and $z = 28$ cm over the twelve analyzed peak groupings is an average of $\Delta N_e = 40\%$ with a standard deviation of $\sigma = 16\%$.

To support the above analysis of density gradient scale lengths, it is necessary to assess the validity of the assumption that adjacent peaks correspond to a discrete intersection of the pinch centroid and the ZaP-HD center axis flowing downstream with the bulk plasma flow. This can be assessed by using the interferometer as a time-of-flight probe by the same method demonstrated by Figure 4.8 as described in Section 4.3. For the twelve sets of peaks analyzed to produce the gradient scale length data in Table 5.1, the mean peak transit velocities and corresponding standard deviations are calculated and reported in Table 5.2.

Window	Mean v_z $[km/s]$	Standard Deviation σ $[km/s]$
$z = 21$ cm to $z = 23.3$ cm	105	26
$z = 23.3$ cm to $z = 25.6$ cm	95	33
$z = 25.6$ cm to $z = 28$ cm	109	32

Table 5.2: Table showing the mean density peak transit velocity v_z and corresponding standard deviation σ for each of the three distance intervals between interferometer chords.

From Table 5.2, it can be seen that the range in $v_z \pm \sigma$ is spanned by the lowest possible value of $v_z - \sigma = 62$ km/s for the second interval, and the largest possible value of $v_z + \sigma = 141$ km/s for the third interval. This entire range of velocity values falls within the expected range of velocities as measured by ion doppler spectroscopy [40]. This information strongly supports the assumptions made for analyzing adjacent peaks in density as measurements of the chord-integrated density at the pinch centroid.

5.2 Axial Evolution of Magnetic Field Strength

Section 5.1 presents that the pinch density does decrease as the plasma flows downstream through the ZaP-HD assembly region. To gain a better understanding of why this decrease might be occurring, the behavior of other plasma parameters which relate to plasma density are evaluated. The pinch is compressed by the axial current through the plasma. Therefore, a decrease in density could potentially correspond with a decrease in pinch current which occurs over the length of the pinch axis, due to plasma diffusing and creating paths for a fraction of the total current density to be diverted to the walls of the outer electrode before reaching the end wall. In terms of what can be observed with available diagnostics, this would result in a downstream decrease in magnetic field magnitudes measured by magnetic field probes along the length of the assembly region. As mentioned in Section 4.4, 8-probe azimuthal arrays located at $z = 15,\ 30,\ 45\ cm$ provided a significant amount of data as was demonstrated by pulse 250424020 in Figure 4.17. Aside from pulse 250424020, this data from ten additional pulses, as shown in Appendix A, is considered in this analysis.

To characterize the change in magnetic field as the plasma flows downstream, magnetic field probe data is azimuthally averaged and time averaged over a window of $t = 20 - 100\ \mu s$ for each of the three array locations. This is done by taking the average magnetic field measurement over time between 20 μs and 100 μs for each probe, then averaging this value over all probes at each z location. Then, for each pulse included in this analysis, percentage decreases in these average magnetic field values are calculated for the distance windows $z = 15 - 30\ \mu s$ and $z = 30 - 45\ \mu s$ between probe arrays. The average percent decreases between the 11 pulses considered, and their respective standard deviations, are reported in Table 5.3.

From these results, it is seen that the magnetic field decreases by a magnitude of roughly 18% over the axial window of $Z = 15 - 30\ cm$. This supports the decrease in density observed by the interferometer over the axial window of $z = 21 - 28\ cm$. For the axial window of $z = 30 - 45\ cm$, there is a measured increase of 13%. As stated in Section 4.4, this is due

Window	Mean Percent Decrease [%]	Standard Deviation σ [%]
$z = 15\ cm$ to $z = 30\ cm$	18.2	2.2
$z = 30\ cm$ to $z = 45\ cm$	-13.0	5.1

Table 5.3: Table showing the mean percent change in magnetic field strength and corresponding standard deviation σ for each of the two distance intervals between 8-probe arrays for the $20 - 100\ \mu s$ time averaging window. A negative decrease percentage will correspond to an increase in measured magnitude. Pulses contributing to this table are numbers 006-010, 015-017, and 019-021 taken on April 24th of 2025. These pulse numbers are selected as they were taken with the same operational parameters as the density data discussed in Section 5.1, specifically the 9 kV acceleration discharge and the 8 kV compression discharge. These pulse numbers are non-sequential. The gap between 010 and 015 is due to a nominal pause in operations followed by gradually ramping the machine back up to high power. The gap between 017 and 019 is due to a capacitor bank charging circuit anomaly which severely altered the behavior of pulse 018.

to plasma stagnation occurring near the end wall.

Chapter 6

CONCLUSIONS

6.1 Functionality of the Unequal Path Length Interferometer

6.1.1 Single-Pass

The density measurements presented in Section 4.3 taken using the single-pass configuration described in Section 3.7.2 show that the HeNe interferometer used on the ZaP-HD experiment can produce useful data in an optical setup which gives the scene and reference beams unequal path lengths. No fine-tuning of path lengths to reach a local maximum of Lissajous figure radius was conducting during the alignment setup to record these density measurements. Chords were aligned as was convenient to avoid interfering with other diagnostics, and the resulting Lissajous radii ranged between 25 mV and 80 mV. All chords had path length differences exceeding two meters, which is outside of the range of path length differences demonstrated in the benchtop proof-of-concept experiment mentioned in Section 3.7. This investigation went a step beyond simply proving that the HeNe interferometer is capable of functioning with unequal path lengths. This proves that that the system is sufficiently robust against path length differences to enable significantly more flexibility in optical setup than previously assumed. This simplifies the implementation of HeNe interferometry on plasma physics experiments which require frequent changes in measurement location within space-constrained optical setups.

6.1.2 Double-Pass

The implementation of the double-pass configuration of the interferometer, as described in Section 3.7.3, was not as successful as the single-pass configuration. There are several possible causes for this, and the most likely explanation for the observed failure is a combination of all of these causes. The most obvious contributor is the scene beam experiencing greater

parasitic attenuation from the optical setup than the single-pass configuration. Requiring two passes through a beam splitter to achieve a collinear return path, plus doubling the passages through the vacuum chamber windows, means the scene beam in the double pass configuration carries only 22% of the incident beam power of the scene beam in the single-pass configuration at the point of recombination with the reference beam. A spherically concave mirror was used as the return mirror with the goal of compensating for this attenuation by focusing the beam down to a smaller incident diameter, which would have ideally resulted in a higher power density at the photodetector. It is believed that the selected two-meter radius of curvature for the spherical mirrors was less than optimal for the setup, as the incident beams were often overexpanded to a larger incident diameter than desired at the photodetector. This setup resulted in Lissajous figures typically achieving radii of 5 mV to 20 mV with characteristic noise levels of approximately ± 2 mV. This low signal-to-noise ratio, combined with the fact that two passes through the plasma will double the fringe jumps for a given density, resulted in recording $\Delta\phi(t)$ data which could not reliably yield plasma density measurements.

6.2 Characterization of Axial Density Decrease

The analysis of the chord-integrated density measurements described in Section 5.1 evaluated the gradient scale lengths of the plasma density over three adjacent axial distance intervals, $z = 21 - 23.3$ cm, $z = 23.3 - 25.6$ cm, and $z = 25.6 - 28$ cm. This analysis revealed that the most significant decrease in density occurred within the third interval, with $z = 25.6 - 28$ cm exhibiting a gradient scale length of 14.6 ± 7.1 cm. The first interval, $z = 21 - 23.3$ cm, had the 2nd shortest scale length at 22.8 ± 15.8 cm. The interval in between, $z = 23.3 - 25.6$ cm, showed a scale length of 31.7 ± 50.0 cm, which indicates a significantly larger shot-to-shot variance than the other two intervals. In addition to the gradient scale length calculations, the overall average density decrease between $z = 21$ cm and $z = 28$ cm was observed to be $40 \pm 16\%$. This analysis was conducted under the assumption that observed density peaks corresponded to radially displaced sections of the pinch producing periodic intersections between the pinch centroid and the interferometer

scene beams. This assumption was supported by observed peak transit times agreeing with expected plasma flow velocities.

Measurements from magnetic field probe arrays were used to calculate the average relative decrease in magnetic field magnitude between $z = 15\ cm$ and $z = 30\ cm$, yielding the result of $\Delta B_\theta = 18 \pm 2\%$. The Bennett equilibrium profile in Section 1.2 predicts that the magnetic field B_θ will scale linearly with the plasma current, and electron density n_e will scale with the plasma current squared. Applying this relationship, a magnetic field decrease of 18% should result in a density decrease of 33%, which falls within the observed range of $40 \pm 16\%$ measured by the interferometer.

To summarize the findings of this investigation, interferometer measurements show a strong trend of density decreasing as a function of distance traveled downstream by the plasma. These measurements are corroborated by magnetic field probe measurements, suggesting that the density decrease is due to a fraction of the current density in the pinch attaching to the internal radius of the outer electrode upstream of the end wall. It is important to note that one significant caveat to these findings is that the measurements recorded for this study were taken using an off-nominal electrode configuration in the ZaP-HD device, as described in Section 4.2. This configuration fundamentally changes the behavior of the initial current sheet at the beginning of a pulse.

6.3 Suggested Future Work

6.3.1 Refining the Interferometer

The optical design of the double-pass configuration must be improved to achieve larger signal-to-noise ratios. The attenuation of the scene beam due to two passes through the ZaP-HD rectangular windows, and two passes through a beam splitter to ensure a collinear return path, must be compensated for. New spherical return mirrors should be selected, with focal lengths chosen specifically to achieve a scene beam incident diameter which matches

the reference beam as the inlet of the photodetector. This should be done on a chord-by-chord basis, rather than selecting one focal length which will be best for the average chord setup.

Additionally, a higher spatial resolution of the HeNe interferometer may be achieved using smaller optics. Decreasing turning mirror and pickoff mirror sizes from 25.4 mm diameter to 12 mm diameter will enable tighter scene beam groupings. This would provide opportunities to observe time-resolved plasma dynamics at smaller spatial scales.

As long as the interferometer is limited to four chords, the aforementioned improvement to spatial resolution will result in a smaller region of the pinch being measured. To improve spatial resolutions over a fixed-size region of the ZaP-HD device, more chords will be required. This will require additional optics, photodetectors, mixer-splitter boxes, and transient recorder digitizer modules with two channels per additional chord.

6.3.2 Additional Measurements and Analysis

Four-Chord Axial Survey

The fine-mesh axial survey configuration for which data was presented in Section 4.3 should be used to record measurements along more 7 cm axial distance ranges. Implementing this configuration somewhere between the tip of the nosecone and $z = 20$ cm will provide insight on plasma density behaviors before significant density decreases are observed. Implementing this configuration anywhere between $z = 30$ cm and the ZaP-HD end wall would produce valuable information on the effects of plasma stagnation at the downstream end of the assembly region.

Radial Disturbance Characterization

The measurements taken using the "2+2" configuration described in Section 4.5 should be repeated with an interferometer configuration which provides a higher signal-to-noise ratio than was achieved during this study. This task may be performed by implementing the single-pass configuration, or addressing the problems with the double-pass configuration as suggested in Section 6.3.1. Once this task is completed, the configuration should be iterated on with varying axial spacings and impact parameters between the four chords, to measure the characteristic sizes of radial disturbances in the plasma flow.

Equilibrium Evolution Measurements

Cross-sectional profiles of the plasma density should be measured using the multichord configuration illustrated in Figure 6.1. This will enable better estimates on the characteristic size of the ZaP-HD pinch, and enable verification of the predictions of the Bennett equilibrium profile.

6.3.3 ZaP-HD Electrode Geometry

The investigation described in this thesis, as well as the future investigations described in Section 6.3.2, should be repeated for two additional ZaP-HD electrode configurations. The first repeat study should be conducted with the ZaP-HD device returned to the nominal electrode configuration, with the tip of the nosecone being flush with the end of the middle electrode. This study will establish a set of baseline measurements to compare other electrode configurations to. The next repeat study should be conducted with the tip of the nosecone displaced upstream from the nominal location, rather than downstream. This study will provide insight on the effects of the current sheet acceleration vector being directed radially inward to a higher degree than the nominal configuration as the plasma transitions between the acceleration region and the assembly region.

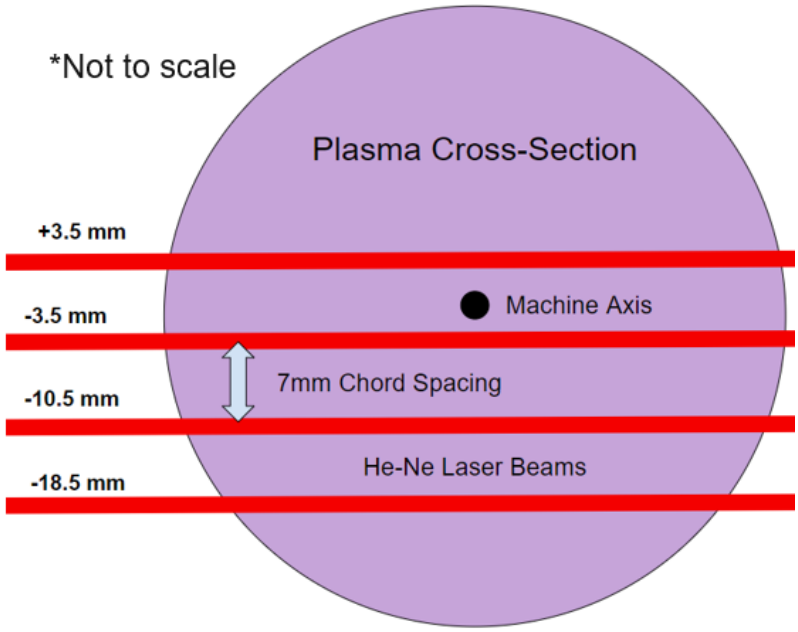

Figure 6.1: Illustration demonstrating a possible arrangement of HeNe interferometer scene beams to measure the cross-sectional equilibrium profile of the pinch.

BIBLIOGRAPHY

[1] Eleanor Forbes. *Diagnostic development and plasma-material interaction studies on the ZaP-HD device*. PhD thesis, University of Washington, 2020.

[2] Elliot Montoya. Unequal path length interferometry for zap-hd flow z-pinch plasma experiment. In *Region VI Student Conference*. AIAA, 2025.

[3] Francis William Aston. Mass-spectra and atomic weights. *Journal of the Chemical Society, Transactions*, 119:677–687, 1921.

[4] Arthur Stanley Eddington. Constitution of the stars. *The Scientific Monthly*, 43(5):385–395, 1936.

[5] Eugen Merzbacher. The early history of quantum tunneling. *Physics Today*, 55(8):44–49, 2002.

[6] Marcus Laurence Elwin Oliphant, Paul Harteck, and Ernest Rutherford. Transmutation effects observed with heavy hydrogen. *Proceedings of the Royal Society of London. Series A, Containing Papers of a Mathematical and Physical Character*, 144(853):692–703, 1934.

[7] Eric G Adelberger, A García, RG Hamish Robertson, KA Snover, AB Balantekin, K Heeger, MJ Ramsey-Musolf, D Bemmerer, A Junghans, CA Bertulani, J-W Chen, H Costantini, P Prati, M Couder, E Uberseder, M Wiescher, R Cyburt, B Davids, SJ Freedman, M Gai, D Gazit, L Gialanella, G Imbriani, U Greife, M Hass, WC Haxton, T Itahashi, K Kubodera, K Langanke, D Leitner, M Leitner, P Vetter, L Winslow, LE Marcucci, T Motobayashi, A Mukhamedzhanov, RE Tribble, Kenneth Nollett, FM Nunes, T-S Park, PD Parker, R Schiavilla, EC Simpson, C Spitaleri, F Strieder, H-P Trautvetter, K Suemmerer, and S Typel. Solar fusion cross sections. II. the pp chain and CNO cycles. *Reviews of Modern Physics*, 83(1):195–245, 2011.

[8] U Shumlak, CS Adams, JM Blakely, B-J Chan, RP Golingo, SD Knecht, BA Nelson, RJ Oberto, MR Sybouts, and GV Vogman. Equilibrium, flow shear and stability measurements in the z-pinch. *Nuclear Fusion*, 49(7):075039, 2009.

[9] U Shumlak and NF Roderick. Mitigation of the rayleigh–taylor instability by sheared axial flows. *Physics of Plasmas*, 5(6):2384–2389, 1998.

[10] Frank J Wessel, Paul Ney, Radu Presura, et al. Fusion in a staged z-pinch. *IEEE Transactions on Plasma Science*, 43(8):2463–2468, 2015.

[11] NF Roderick, TW Hussey, RJ Faehl, and RW Boyd. Two-dimensional simulation of the hydromagnetic rayleigh-taylor instability in an imploding foil plasma. *Applied Physics Letters*, 32(5):273–275, 1978.

[12] S. Chandrasekhar. *Hydrodynamic and Hydromagnetic Stability*. Oxford University Press, 1961.

[13] Willard H Bennett. Magnetically self-focussing streams. *Physical Review*, 45(12):890, 1934.

[14] Jeffrey P Freidberg. Ideal magnetohydrodynamic theory of magnetic fusion systems. *Reviews of Modern Physics*, 54(3):801, 1982.

[15] Sean D Knecht, Raymond P Golingo, Brian A Nelson, and Uri Shumlak. Calculation of the equilibrium evolution of the zap flow z-pinch using a four-chord interferometer. *IEEE Transactions on Plasma Science*, 43(8):2469–2479, 2015.

[16] U Shumlak and CW Hartman. Sheared flow stabilization of the m= 1 kink mode in z pinches. *Physical Review Letters*, 75(18):3285, 1995.

[17] RP Golingo, U Shumlak, and BA Nelson. Formation of a sheared flow z pinch. *Physics of Plasmas*, 12(6), 2005.

[18] Raymond Golingo. *Formation of a Sheared Flow Z-Pinch*. PhD thesis, University of Washington, 2003.

[19] U Shumlak, RP Golingo, BA Nelson, and DJ Den Hartog. Evidence of stabilization in the z-pinch. *Physical Review Letters*, 87(20):205005, 2001.

[20] K Tummel, DP Higginson, AEW Schmidt, DT Offermann, DR Welch, RE Clark, U Shumlak, BA Nelson, RP Golingo, and HS McLean. Kinetic simulations of sheared flow stabilization in high-temperature z-pinch plasmas. *Physics of Plasmas*, 26(6), 2019.

[21] Uri Shumlak. Z-pinch fusion. *Journal of Applied Physics*, 127(20), 2020.

[22] B Levitt, C Goyon, JT Banasek, SC Bott-Suzuki, C Liekhus-Schmaltz, ET Meier, LA Morton, A Taylor, WC Young, BA Nelson, DA Sutherland, M Quinley, AD Stepanov, JR Barhydt, P Tsai, KD Morgan, N van Rossum, AC Hossack, TR Weber, WA McGehee, P Nguyen, A Shah, S Kiddy, M Van Patten, AE Youmans, DP Higginson, HS McLean, GA Wurden, and U Shumlak. Elevated electron temperature coincident with observed fusion reactions in a sheared-flow-stabilized z pinch. *Physical Review Letters*, 132(15):155101, 2024.

[23] Y Zhang, U Shumlak, BA Nelson, RP Golingo, TR Weber, AD Stepanov, EL Claveau, EG Forbes, ZT Draper, JM Mitrani, HS McLean, KK Tummel, DP Higginson, and CM Cooper. Sustained neutron production from a sheared-flow stabilized z pinch. *Physical Review Letters*, 122(13):135001, 2019.

[24] U Shumlak, BA Nelson, EL Claveau, EG Forbes, RP Golingo, MC Hughes, RJ Oberto, MP Ross, and TR Weber. Increasing plasma parameters using sheared flow stabilization of a z-pinch. *Physics of Plasmas*, 24(5), 2017.

[25] A. Kramida, Yu. Ralchenko, J. Reader, and and NIST ASD Team. NIST Atomic Spectra Database (ver. 5.12), [Online]. Available: `https://physics.nist.gov/asd` [2016, January 31]. National Institute of Standards and Technology, Gaithersburg, MD., 2024.

[26] A.A. Khairi, W. Wilhere, and U. Shumlak. A two-color pyrometer for measuring electrode surface temperature on the zap-hd sheared-flow-stabilized z-pinch device. American Physical Society Division of Plasma Physics, October 2024.

[27] Bonghan Kim. *Multi-chord Heterodyne Quadrature Interferometry Measurement of the FuZE Sheared Flow Z - Pinch Plasma*. Master's thesis, University of Washington, 2018.

[28] Donald Gary Swanson. *Plasma waves*. CRC Press, 2020.

[29] Timothy Lloyd. *Comparison of diagnostics for determining z pinch centroid in the zap-hd experiment*. Master's thesis, University of Washington, 2022.

[30] CJ Buchenauer and AR Jacobson. Quadrature interferometer for plasma density measurements. *Review of Scientific Instruments*, 48(7):769–774, 1977.

[31] Deepak Kumar and Paul M Bellan. Heterodyne interferometer with unequal path lengths. *Review of Scientific Instruments*, 77(8), 2006.

[32] Alexander Harrison Card. *Implementation of an unequal path length, heterodyne interferometer on the MOCHI LabJet experiment*. Master's thesis, University of Washington, 2017.

[33] H. Furey and U. Shumlak. Spatiotemporal evolution of electron density in the ZaP-HD sheared-flow-stabilized z-pinch, November 2023. Poster Presented at 65th Annual Meeting of APS-DPP.

[34] Sean D Knecht, Weston Lowrie, and Uri Shumlak. Effects of a conducting wall on z-pinch stability. *IEEE Transactions on Plasma Science*, 42(6):1531–1543, 2014.

[35] AD Stepanov, U Shumlak, HS McLean, BA Nelson, EL Claveau, EG Forbes, TR Weber, and Y Zhang. Flow z-pinch plasma production on the fuze experiment. *Physics of Plasmas*, 27(11), 2020.

[36] U Shumlak, BA Nelson, RP Golingo, SL Jackson, EA Crawford, and DJ Den Hartog. Sheared flow stabilization experiments in the zap flow z pinch. *Physics of Plasmas*, 10(5):1683–1690, 2003.

[37] U Shumlak, J Chadney, RP Golingo, DJ Den Hartog, MC Hughes, SD Knecht, W Lowrie, VS Lukin, BA Nelson, RJ Oberto, et al. The sheared-flow stabilized z-pinch. *Fusion Science and Technology*, 61(1T):119–124, 2012.

[38] U Shumlak, ET Meier, and BJ Levitt. Fusion gain and triple product for the sheared-flow-stabilized z pinch. *Fusion Science and Technology*, 80(1):1–16, 2024.

[39] James M Mitrani, Drew P Higginson, Zack T Draper, Jonathan Morrell, Lee A Bernstein, Elliot L Claveau, Christopher M Cooper, Eleanor G Forbes, Ray P Golingo, Brian A Nelson, Andrea E Schmidt, Anton D Stepanov, Tobin R Weber, Yue Zhang, Harry S McLean, and Uri Shumlak. Measurements of temporally-and spatially-resolved neutron production in a sheared-flow stabilized z-pinch. *Nuclear Instruments and Methods in Physics Research Section A: Accelerators, Spectrometers, Detectors and Associated Equipment*, 947:162764, 2019.

[40] EL Claveau, U Shumlak, BA Nelson, EG Forbes, AD Stepanov, TR Weber, Y Zhang, and HS McLean. Plasma exhaust in a sheared-flow-stabilized z pinch. *Physics of Plasmas*, 27(9), 2020.

Appendix A

ADDITIONAL MAGNETIC FIELD PROBE DATA

Plots below show the magnetic field probe data which contributed to the data presented in Table 5.3.

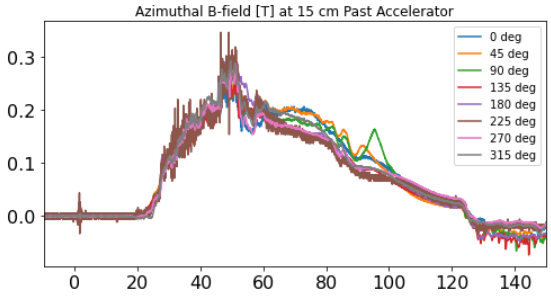

Figure A.1: $z = 15$ cm, Pulse 250424006

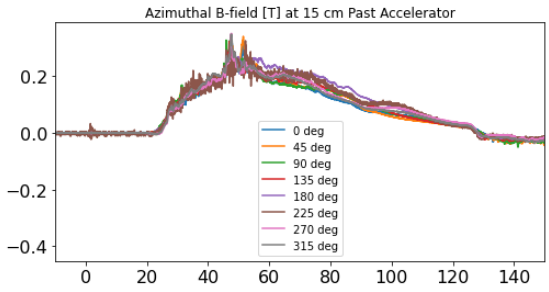

Figure A.2: $z = 15$ cm, Pulse 250424007

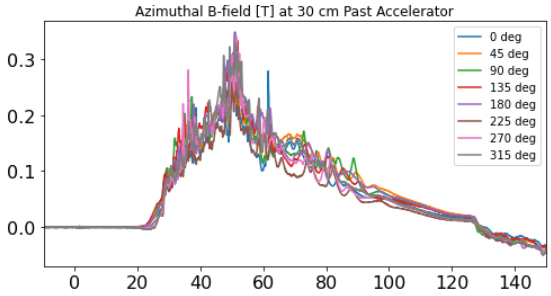

Figure A.3: $z = 30$ cm, Pulse 250424006

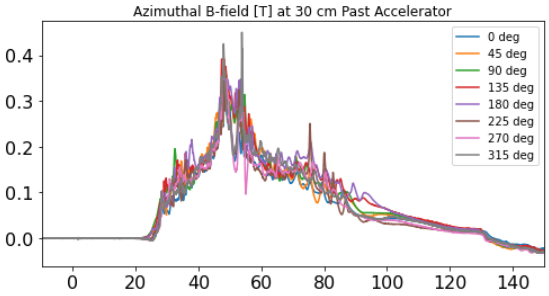

Figure A.4: $z = 30$ cm, Pulse 250424007

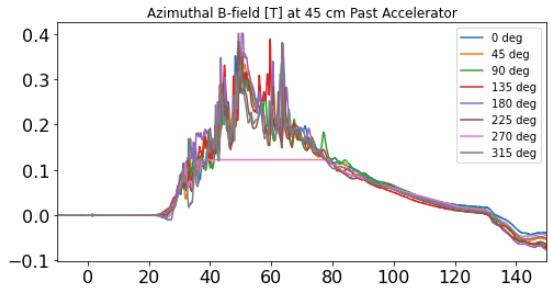

Figure A.5: $z = 45$ cm, Pulse 250424006

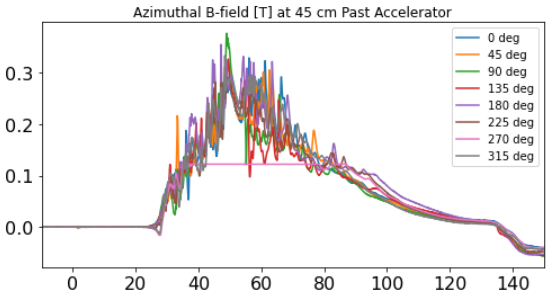

Figure A.6: $z = 45$ cm, Pulse 250424007

Figure A.7: Time-resolved magnetic field plots for pulse 250424006 (Left) and pulse 250424007 (Right)

.

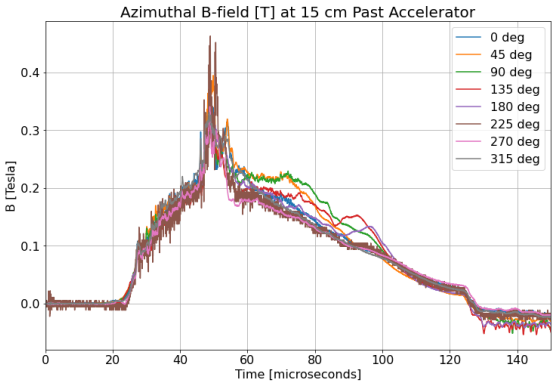

Figure A.8: $z = 15$ cm, Pulse 250424008

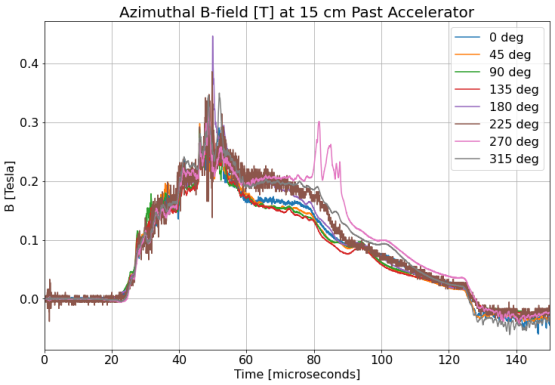

Figure A.9: $z = 15$ cm, Pulse 250424009

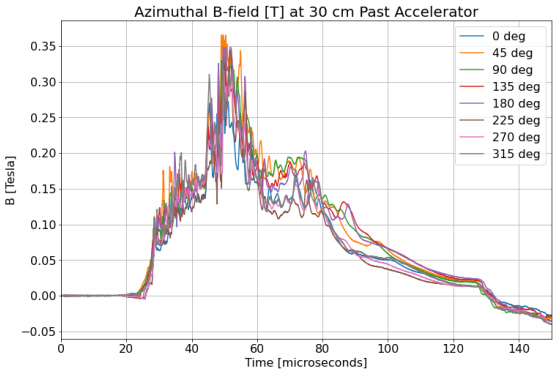

Figure A.10: $z = 30$ cm, Pulse 250424008

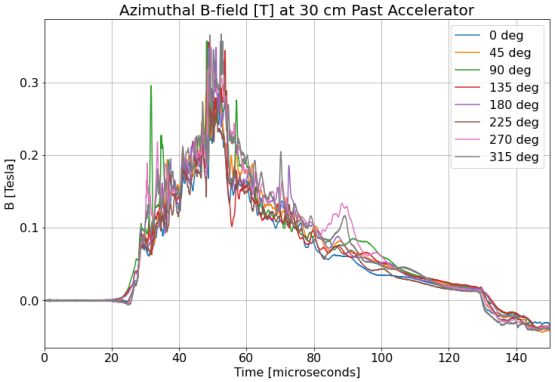

Figure A.11: $z = 30$ cm, Pulse 250424009

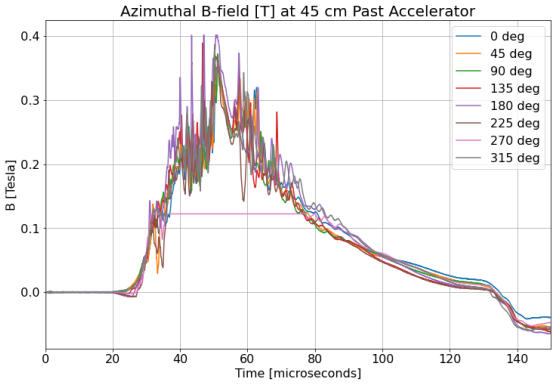

Figure A.12: $z = 45$ cm, Pulse 250424008

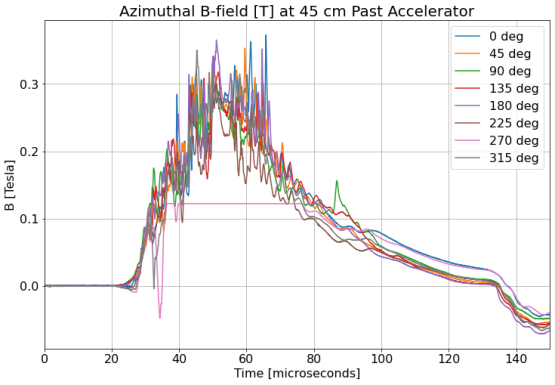

Figure A.13: $z = 45$ cm, Pulse 250424009

Figure A.14: Time-resolved magnetic field plots for pulse 250424008 (Left) and pulse 250424009 (Right)

.

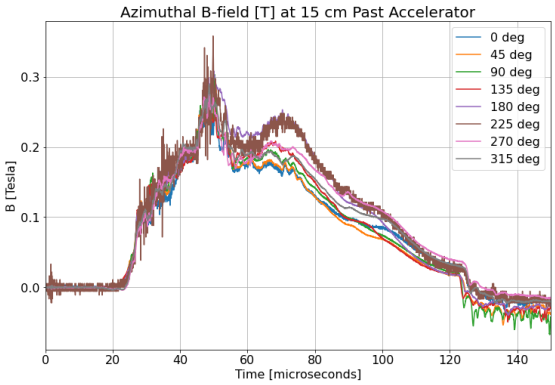

Figure A.15: $z = 15$ cm, Pulse 250424010

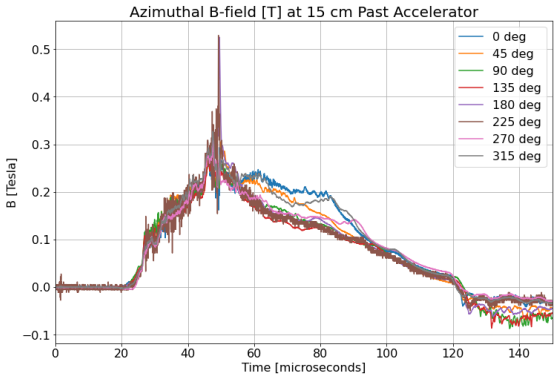

Figure A.16: $z = 15$ cm, Pulse 250424015

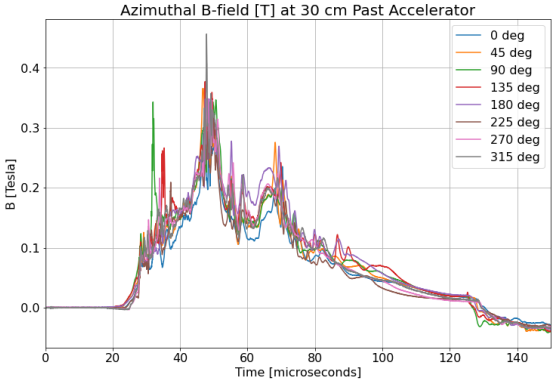

Figure A.17: $z = 30$ cm, Pulse 250424010

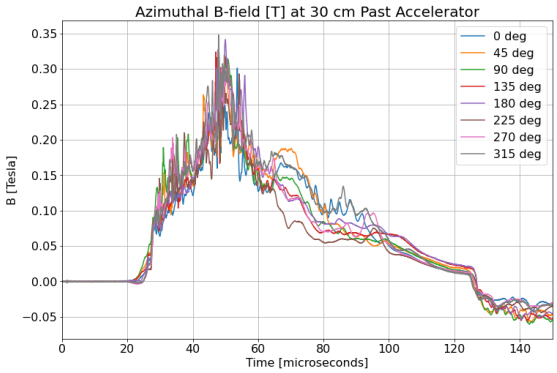

Figure A.18: $z = 30$ cm, Pulse 250424015

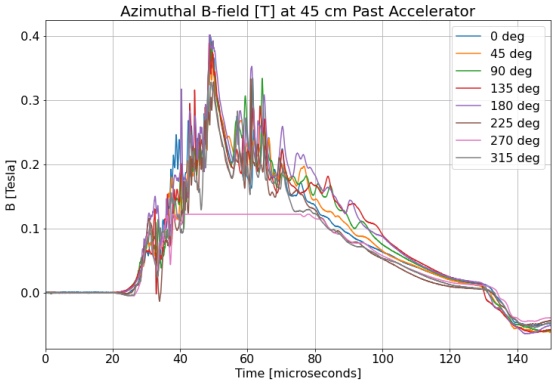

Figure A.19: $z = 45$ cm, Pulse 250424010

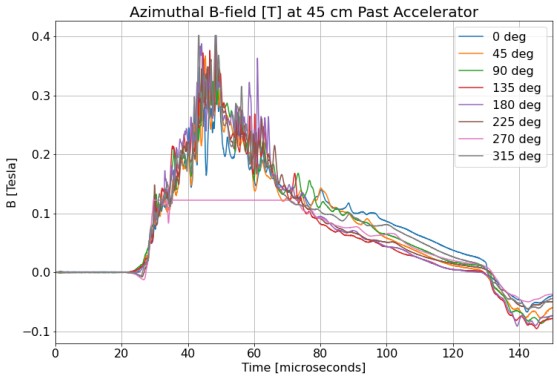

Figure A.20: $z = 45$ cm, Pulse 250424015

Figure A.21: Time-resolved magnetic field plots for pulse 250424010 (Left) and pulse 250424015 (Right)

.

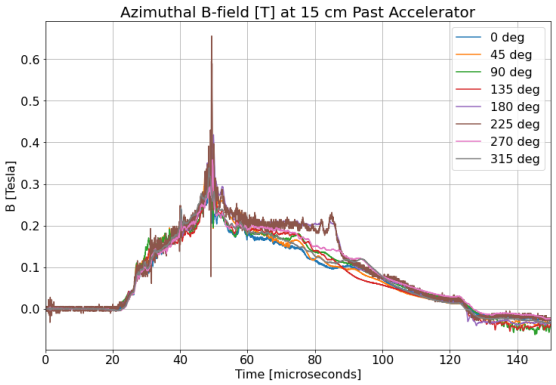

Figure A.22: $z = 15$ cm, Pulse 250424016

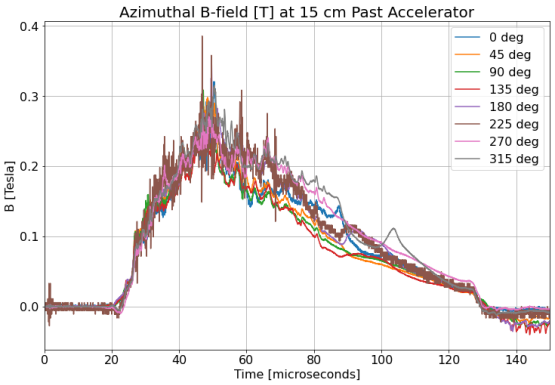

Figure A.23: $z = 15$ cm, Pulse 250424017

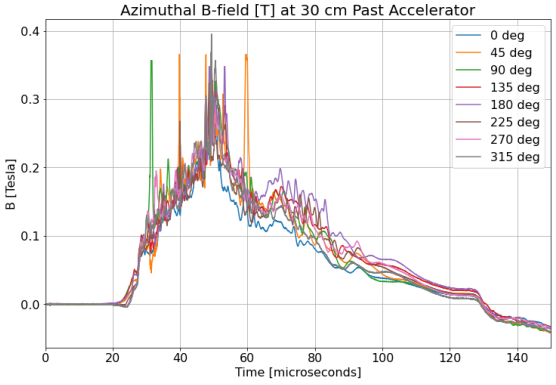

Figure A.24: $z = 30$ cm, Pulse 250424016

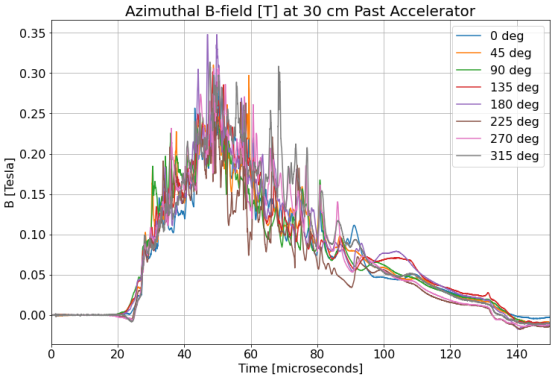

Figure A.25: $z = 30$ cm, Pulse 250424017

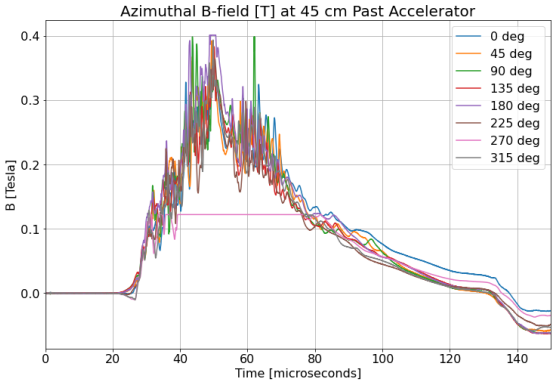

Figure A.26: $z = 45$ cm, Pulse 250424016

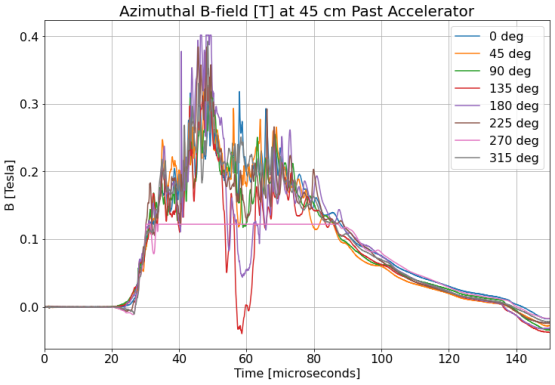

Figure A.27: $z = 45$ cm, Pulse 250424017

Figure A.28: Time-resolved magnetic field plots for pulse 250424016 (Left) and pulse 250424017 (Right)

.

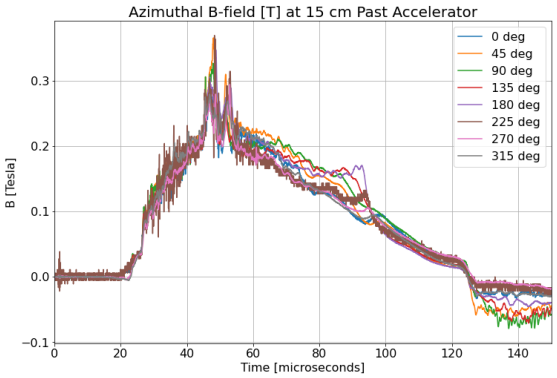

Figure A.29: $z = 15$ cm, Pulse 250424019

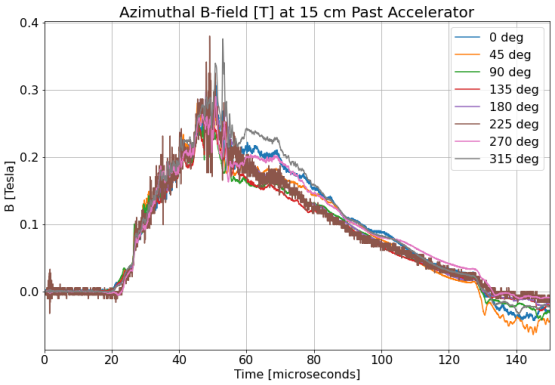

Figure A.30: $z = 15$ cm, Pulse 250424021

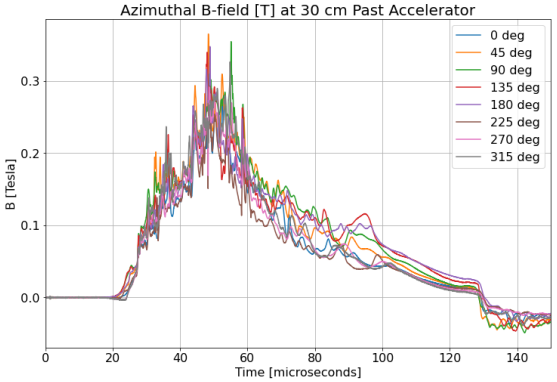

Figure A.31: $z = 30$ cm, Pulse 250424019

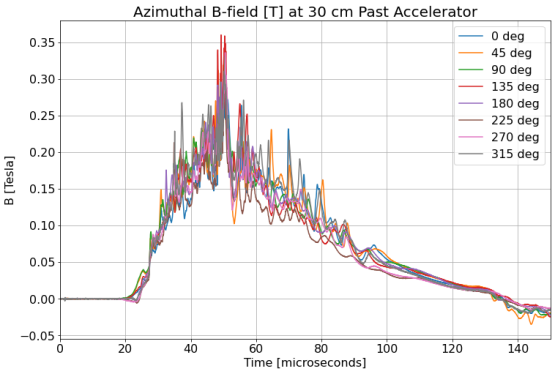

Figure A.32: $z = 30$ cm, Pulse 250424021

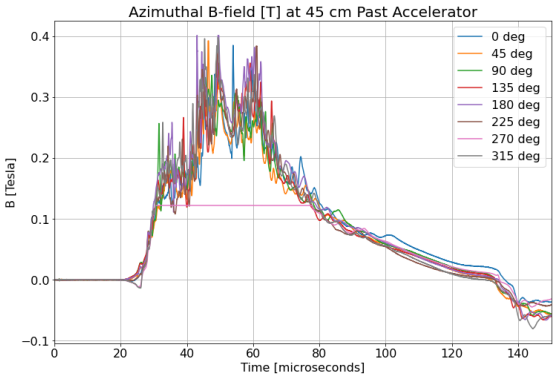

Figure A.33: $z = 45$ cm, Pulse 250424019

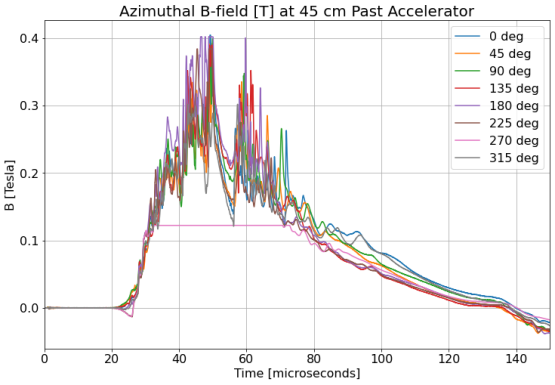

Figure A.34: $z = 45$ cm, Pulse 250424021

Figure A.35: Time-resolved magnetic field plots for pulse 250424019 (Left) and pulse 250424021 (Right)

.

Appendix B

PYTHON SCRIPTS FOR HENE INTERFEROMETER ANALYSIS

```
    import numpy as np
from sys import argv
from MDSplus import Tree
import MDSplus as MDS
import matplotlib.pyplot as plt
from MDSplus import Connection
from scipy.optimize import least_squares
import scipy
import pandas as pd
import csv


def treepull(shotnum):
    conn = Connection('zappa.zap')
    conn.openTree('zaphd', shotnum)
    #t = MDS.Tree('zaphd', shotnum)
    return conn#, t
#load HeNe trig sig data
#imports cosRaw, sinRaw, and time_raw signal given chord, refShotnum, and tree
def loadIFdata(chord, conn):
    cosRaw =conn.get(r'\cos%d' % chord).getData().data()
    sinRaw =conn.get(r'\sin%d' % chord).getData().data()
    time_Raw =conn.get('dim_of(\cos2)').getData().data()
    return cosRaw, sinRaw, time_Raw
#load plasma and machine current data
```

```
def␣loadcurrents(conn):
␣␣␣␣I_P␣=␣conn.get('\i_p').getData().data()␣#plasma␣current
␣␣␣␣I_C␣=␣conn.get('\i_c').getData().data()␣#compression␣current
␣␣␣␣I_A␣=␣conn.get('\i_a').getData().data()␣#acceleration␣current
␣␣␣␣return␣I_P,␣I_C,␣I_A
#find␣plasma␣end␣time␣by␣I_p␣zero␣crossing
def␣plasma_end(time,␣I_P,␣comp_delay=2e-5):
␣␣␣␣comp_idx␣=␣np.searchsorted(time,␣comp_delay)␣#compression␣trigger␣index
␣␣␣␣for␣i␣in␣range(comp_idx␣+␣1,␣len(I_P)):
␣␣␣␣␣␣␣␣prev_val␣=␣I_P[i-1]
␣␣␣␣␣␣␣␣curr_val␣=␣I_P[i]
␣␣␣␣␣␣␣␣if␣prev_val␣>␣0␣and␣curr_val␣<␣0:
␣␣␣␣␣␣␣␣␣␣␣␣plasma_end_idx␣=␣i
␣␣␣␣␣␣␣␣␣␣␣␣break
␣␣␣␣plasma_end_time␣=␣time[plasma_end_idx]
␣␣␣␣comp_trig_time␣=␣time[comp_idx]
␣␣␣␣return␣plasma_end_idx,␣plasma_end_time,␣comp_idx,␣comp_trig_time

def␣sigs_noplasma(cosraw,␣sinraw,␣plasma_end_idx,␣comp_idx):
␣␣␣␣cos_pre␣=␣cosraw[0:comp_idx]
␣␣␣␣sin_pre␣=␣sinraw[0:comp_idx]
␣␣␣␣cos_post␣=␣cosraw[plasma_end_idx:-1]
␣␣␣␣sin_post␣=␣sinraw[plasma_end_idx:-1]
␣␣␣␣cos_noplasma␣=␣[*cos_pre,␣*cos_post]
␣␣␣␣sin_noplasma␣=␣[*sin_pre,␣*sin_post]
␣␣␣␣return␣cos_pre,␣sin_pre,␣cos_noplasma,␣sin_noplasma

def␣fit_circle(x,␣y):
␣␣␣␣A_matrix␣=␣np.vstack([x,␣y,␣np.ones(len(x))]).T
␣␣␣␣b_vector␣=␣(np.array(x))**2␣+␣(np.array(y))**2
```

```
    a, b, c = np.linalg.lstsq(A_matrix, b_vector, rcond=None)[0]

    h_initial = a / 2
    k_initial = b / 2
    r_initial = np.sqrt(c + h_initial**2 + k_initial**2)

    def residuals(parameters, x_vals, y_vals):
        h, k, r = parameters
        return np.sqrt((x_vals - h)**2 + (y_vals - k)**2) - r

    initial_guess = [h_initial, k_initial, r_initial]
    result = least_squares(residuals, initial_guess, args=(x,y))

    h, k, r = result.x
    return (h, k, r)

def calc_initial_phase(cos_SubBase, sin_SubBase, zero_idx):
    # Finding initial phase
    #phaseInitial = np.arctan2(sin_SubBase[0], cos_SubBase[0])
    phaseInitial = np.arctan2(sin_SubBase[zero_idx],
                              cos_SubBase[zero_idx]) #t=0 index
    # Rotate the sin and cos signal by - initial phase
    return phaseInitial
#rotate xArray, yArray CW by angleRad
def rotate2d(xArray, yArray, angleRad):
    xArray_new = xArray * np.cos(angleRad) + yArray * np.sin(angleRad)
    yArray_new = -xArray * np.sin(angleRad) + yArray * np.cos(angleRad)
    return xArray_new, yArray_new
#Aria's fringe jump correction function
def get_jumpcorr(phase, radius, jump=np.pi, ignoreZeroR=False):
```

```
    '''
    when change in value between data is greater than threshold it
    increments the jump_correction list
    '''
    length = len(phase)
    total_correction = 0
    jump_correction = np.zeros(length)
    zero_rad_idx = np.zeros(length)
    for i in range(1, length-1):
        delta_phi = phase[i] - phase[i-1]
        #delta_2step = (phase[i]-phase[i-1]) + (phase[i+1] - phase[i])
        if ignoreZeroR and radius[i] < 0.01:
            zero_rad_idx[i] = 1
            #pass
        elif delta_phi > jump:
            total_correction += 1
        elif delta_phi < -jump:
            total_correction -= 1
        # elif delta_2step > 2*jump:
        #     total_correction += 1
        # elif delta_2step < -2*jump:
        #     total_correction -= 1
        jump_correction[i] = total_correction
    tot_cor = 1 if total_correction != 0 else 0
    return jump_correction, tot_cor, zero_rad_idx

def get_radius(cos_SubBase, sin_SubBase):
    '''
    calculates radius of lisajou using cos_SubBase, sin_SubBase
    '''
```

```
    radius = np.sqrt(sin_SubBase**2 + cos_SubBase**2)
    return radius

def find_nearest(array, value):
    array = np.asarray(array)
    idx = (np.abs(array - value)).argmin()
    return idx

def linear_function(x, a, b):
    return a * x + b

def dub_boxcar(data, window):
    data = pd.Series(data)
    box1 = data.rolling(window=window).mean()
    box2 = box1.rolling(window=window).mean()
    return box2

def correct_missed_jumps(phase_data, w, n):
    corrected_phase = phase_data.copy()
    total_shift = 0

    jump_index = np.zeros(np.abs(n))
    for k in range(len(jump_index)):
        # Calculate sliding window differences
        window_diffs = np.array([
            np.max(corrected_phase[i:i+w]) - np.min(corrected_phase[i:i+w])
            for i in range(len(corrected_phase) - w)
        ])
        max_jump_start = np.argmax(window_diffs)
        local_window = corrected_phase[max_jump_start:max_jump_start+w+1]
```

```
        local_diffs = np.diff(local_window)
        max_single_step_index = np.argmax(np.abs(local_diffs))

        # Calculate the global index for this maximum single-step change
        jump_index[k] = max_jump_start + max_single_step_index + 1
        #print(jump_index[k])
        jump_index_int = int(jump_index[k])
        print(jump_index_int)
        # Apply the 2*pi correction from this point onward
        shift_dir=-2*np.pi if local_diffs[max_single_step_index]>0 else 2*np.pi
        total_shift += shift_dir
        print(k)
        corrected_phase[jump_index_int:] += shift_dir

    return corrected_phase, total_shift, jump_index

def prep_for_manual(shotnum, conn, chord):
    cosraw, sinraw, time = loadIFdata(chord, conn)
    I_P, I_C, I_A = loadcurrents(conn)
    I_P = I_P*(-1)
    plasma_end_idx, plasma_end_time, comp_idx, comp_time = plasma_end(time,
                                                                      I_P)
    cos_pre, sin_pre, cos_noplasma, sin_noplasma=sigs_noplasma(cosraw, sinraw,
                                                               plasma_end_idx,
                                                               comp_idx)
    cos_offset, sin_offset, radius = fit_circle(cos_noplasma, sin_noplasma)
    #cos_noplasma_suboff = cos_noplasma - cos_offset
    #sin_noplasma_suboff = sin_noplasma - sin_offset
    cos_suboff = cosraw - cos_offset
    sin_suboff = sinraw - sin_offset
```

```
    t_zero_idx = np.searchsorted(time, 0)
    phaseInitial = calc_initial_phase(cos_suboff, sin_suboff, t_zero_idx)
    cos_rotated, sin_rotated = rotate2d(cos_suboff, sin_suboff, phaseInitial)
    phase = np.arctan2(sin_rotated, cos_rotated)

    #shift of Q3 and Q4 coords
    phase_adj = phase

    for i in range(len(phase_adj)):
        if np.sign(sin_rotated[i])<0.:
            phase_adj[i] += 2*np.pi

    jumpfactor = 1
    jump = jumpfactor * np.pi

    radius = get_radius(cos_rotated, sin_rotated)
    jumpcorr_IZR, tot_cor_IZR, zero_rad_idx = get_jumpcorr(phase,
                                                           radius,
                                                           jump=jump,
                                                           ignoreZeroR = False)
    unwrapped_IZR=-1*(phase_adj-jumpcorr_IZR*2*np.pi) #inverted for some reason

    popt_IZR, pcov_IZR = scipy.optimize.curve_fit(linear_function,
                                                  time[0:t_zero_idx],
                                                  unwrapped_IZR[0:t_zero_idx])
    a_opt_IZR, b_opt_IZR = popt_IZR
    vibe_phase_fit_IZR = linear_function(time, a_opt_IZR, b_opt_IZR)
    corrected_phase_IZR = (unwrapped_IZR - vibe_phase_fit_IZR)
```

```
    max_jump_IZR = np.diff(corrected_phase_IZR).max()
    max_jump_ind_IZR = find_nearest(np.diff(corrected_phase_IZR), max_jump_IZR)

    begin_trunc = t_zero_idx - 100
    end_trunc = plasma_end_idx + 1000

    current_scale = np.max(I_P)
    I_P_normed = 4*np.pi * I_P / current_scale

    plasma_end_phase = corrected_phase_IZR[plasma_end_idx]
    missed_jumps = round(plasma_end_phase/(2*np.pi))
    fringe_scan_window = 5

    phase_truncd = corrected_phase_IZR[begin_trunc:end_trunc]
    #phase_truncd = -1*corrected_phase_IZR[begin_trunc:end_trunc]
    time_truncd = time[begin_trunc:end_trunc]
    IPnorm_truncd = I_P_normed[begin_trunc:end_trunc]
    IP_truncd = I_P[begin_trunc:end_trunc]

    return phase_truncd, time_truncd, IP_truncd

def det_disconts(data, threshold):
    diffs = np.diff(data)
    discontinuity_indices = np.where(np.abs(diffs) > threshold)[0] + 1
    directions = np.sign(diffs[discontinuity_indices - 1])
    # -1 for decrease, 1 for increase
    discontinuity_info = np.vstack((discontinuity_indices, directions)).T
    print(``Discontinuity indices and directions:")
    print(discontinuity_info.tolist())
    plt.figure(figsize=(20, 8))
```

```
␣␣␣␣plt.plot(data,␣label='Original␣Data',␣color='blue')
␣␣␣␣#plt.plot(data[700:2700],␣label='Original␣Data',␣color='blue')
␣␣␣␣for␣idx,␣direction␣in␣discontinuity_info:
␣␣␣␣␣␣␣␣color␣=␣'green'␣if␣direction␣==␣1␣else␣'red'
␣␣␣␣␣␣␣␣plt.axvline(x=idx,␣color=color,␣linestyle='--',␣alpha=0.6)
␣␣␣␣plt.title(f'Phase␣with␣Suspected␣Jumps␣(Threshold␣=␣{threshold})')
␣␣␣␣plt.xlabel('Index')
␣␣␣␣plt.ylabel('Phase␣[rad]')
␣␣␣␣plt.legend()
␣␣␣␣plt.grid(True)
␣␣␣␣plt.show()
␣␣␣␣return␣discontinuity_info

def␣filt_disconts(discontinuity_info,␣indices_to_remove):
␣␣␣␣#␣Remove␣specified␣rows␣based␣on␣the␣provided␣index␣list
␣␣␣␣filtered_info␣=␣np.delete(discontinuity_info,␣indices_to_remove,␣axis=0)

␣␣␣␣#␣Print␣the␣updated␣discontinuity␣info␣for␣confirmation
␣␣␣␣print(``Filtered␣Discontinuity␣Info:")
␣␣␣␣print(filtered_info.tolist())

␣␣␣␣return␣filtered_info

def␣apply_corrs(data,␣correction_info,␣correction_value=2*np.pi):
␣␣␣␣#␣Make␣a␣copy␣to␣avoid␣modifying␣the␣original␣data
␣␣␣␣corrected_data␣=␣np.array(data,␣dtype=float)

␣␣␣␣#␣Apply␣corrections␣at␣each␣specified␣index␣with␣appropriate␣direction
␣␣␣␣for␣idx,␣direction␣in␣correction_info:
␣␣␣␣␣␣␣␣idx␣=␣int(np.round(idx))
```

```
␣␣␣␣␣␣␣␣corrected_data[idx:]␣+=␣direction␣*␣correction_value␣*(-1)

␣␣␣␣plt.figure(figsize=(20,␣8))
␣␣␣␣plt.plot(corrected_data,␣label=’Corrected␣Data’,␣color=’blue’)
␣␣␣␣#plt.plot(corrected_data[700:2700],␣label=’Corrected␣Data’,␣color=’blue’)
␣␣␣␣plt.xlabel(’Index’)
␣␣␣␣plt.ylabel(’Phase␣[rad]’)
␣␣␣␣plt.legend()
␣␣␣␣plt.grid(True)
␣␣␣␣plt.show()

␣␣␣␣return␣corrected_data

#one␣problem␣to␣note␣below:␣sometimes␣"uncfit"␣is␣above␣"tvfit",␣need␣to␣add
#check␣to␣switch␣subtraction␣to␣uncfit␣if␣this␣is␣the␣case
#will␣need␣to␣reevaluate␣uncertainty␣calcs␣for␣that␣situation␣as␣well
def␣vibesub(phaseF,␣timeF,␣I_PF):␣#truncd␣vals,␣should␣be␣able␣to␣do␣it␣all?
␣␣␣␣sm_winF␣=␣10
␣␣␣␣smooth_phaseF␣=␣dub_boxcar(phaseF,␣sm_winF)
␣␣␣␣#important␣indices
␣␣␣␣plas_end_idxF,␣plas_end_timeF,␣comp_idxF,␣comp_timeF␣=␣plasma_end(timeF,
␣␣␣␣␣␣␣␣␣␣␣␣␣␣␣␣␣␣␣␣␣␣␣␣␣␣␣␣␣␣␣␣␣␣␣␣␣␣␣␣␣␣␣␣␣␣␣␣␣␣␣␣␣␣␣␣␣␣␣␣␣␣␣␣␣␣␣␣␣␣I_PF)
␣␣␣␣if␣np.sign(np.mean(smooth_phaseF[comp_idxF:plas_end_idxF-1000]))␣<␣0:
␣␣␣␣␣␣␣␣smooth_phaseF␣=␣smooth_phaseF*(-1)
␣␣␣␣#tail␣vibration␣fit
␣␣␣␣tv_fitstart␣=␣find_nearest(
␣␣␣␣␣␣␣␣smooth_phaseF[comp_idxF:(comp_idxF+200)],
␣␣␣␣␣␣␣␣0.05)+comp_idxF␣#good␣enough␣for␣any␣shot␣above␣rampus␣voltages
␣␣␣␣#tv_fitend␣=␣len(time_truncd)␣-␣5␣#lazy,␣not␣consistently␣a␣good␣choice
␣␣␣␣tv_fitend␣=␣plas_end_idxF␣+␣np.argmin(smooth_phaseF[plas_end_idxF:-200])
```

```
    tv_timepts = [timeF[tv_fitstart], timeF[tv_fitend]]
    tv_phasepts = [smooth_phaseF[tv_fitstart], smooth_phaseF[tv_fitend]]
    tv_popt, tv_pcov = scipy.optimize.curve_fit(linear_function,
                                                tv_timepts, tv_phasepts)
    a_tv, b_tv = tv_popt
    tv_fit = linear_function(timeF, a_tv, b_tv)
    #uncertainty fit
    unc_fitstart = tv_fitstart #- 10
    uncfit_end = np.argmin(smooth_phaseF[:plas_end_idxF-200])
    unc_timepts = [timeF[unc_fitstart], timeF[uncfit_end]]
    unc_phasepts = [smooth_phaseF[unc_fitstart], smooth_phaseF[uncfit_end]]
    unc_popt, unc_pcov = scipy.optimize.curve_fit(linear_function,
                                                  unc_timepts, unc_phasepts)
    a_unc, b_unc = unc_popt
    unc_fit = linear_function(timeF, a_unc, b_unc)
    #plot check
    fitfig = plt.figure(figsize=(20,10))
    plt.plot(timeF, smooth_phaseF)
    plt.plot(timeF, tv_fit, label='reported correction')
    plt.plot(timeF, unc_fit, label='conservative correction')
    plt.ylabel('phase [rad]', fontsize=18)
    plt.xlabel('time [s]', fontsize=18)
    plt.axvline(x=plas_end_timeF)
    plt.axvline(x=timeF[tv_fitstart], color='green',
                label='fit bounds', linestyle='--')
    plt.axvline(x=timeF[tv_fitend], color='green', linestyle='--')
    #plt.axvline(x=timeF[uncfit_end], color='green')
    plt.axvline(x=timeF[plas_end_idxF], color='red',
                label='Plasma Current Reversal', linestyle='--')
    plt.legend(fontsize=18)
```

```
    #plt.axvline(x=timeF[comp_idxF], color='red')
    #apply tv correction
    tv_corr = np.zeros(len(smooth_phaseF))
    if tv_fit[-1] < unc_fit[-1]:
        tv_corr[tv_fitstart:] = + tv_fit[tv_fitstart:]
    else:
        tv_corr[tv_fitstart:] = + unc_fit[tv_fitstart:]
        print('uncertainty flag on vibe fit')
    #tv_corr[tv_fitstart:] = + tv_fit[tv_fitstart:]
    phase_tvcorr = smooth_phaseF - tv_corr
    #save uncertainty fit for relevant bounds
    vibe_unc = np.zeros(len(smooth_phaseF))
    vibe_unc[unc_fitstart:] = + unc_fit[unc_fitstart:]
    #plot corrected phase
    corrfig = plt.figure(figsize=(20, 10))
    plt.plot(timeF, phase_tvcorr)
    plt.errorbar(timeF, phase_tvcorr, yerr=(np.abs(tv_corr-vibe_unc)),
                 xerr=None)
    plt.ylabel('phase [rad]', fontsize=18)
    plt.xlabel('time [s]', fontsize=18)
    return phase_tvcorr, vibe_unc

#now converting to density and plot

def NEplot(time_NE, phase_NE, convert=5.61E+20):
    density = phase_NE*convert
    NE_fig = plt.figure(figsize=(20,10))
    plt.plot(time_NE, density)
    return density
```

```
#shotnum = 250508016
shotnum = 250424020
conn = treepull(shotnum)
chord = 4

'''
label "PM" is pre-manual corrections, truncated
'''
PM_phase, PM_time, PM_IP = prep_for_manual(shotnum=shotnum,
                                           conn=conn, chord=chord)

# window = 3
# PM_phase = dub_boxcar(pd.Series(PM_phase), window)

corr_info = det_disconts(PM_phase, 0.7*np.pi)

'''
quick copy+paste lines for analysis
if no jumps:
phase_tvcorr, vibe_unc = vibesub(PM_phase, PM_time, PM_IP)
if no filt needed:
corrphase = apply_corrs(PM_phase, corr_info)

filt = filt_disconts(corr_info, [])
corrphase = apply_corrs(PM_phase, filt)
phase_tvcorr, vibe_unc = vibesub(corrphase, PM_time, PM_IP)

NE_1 = NEplot(PM_time, phase_tvcorr)
NE_2 = NEplot(PM_time, phase_tvcorr)
NE_3 = NEplot(PM_time, phase_tvcorr)
```

```
NE_4 = NEplot(PM_time, phase_tvcorr)
for double pass shots:
NE_1 = NEplot(PM_time, phase_tvcorr, convert=(5.61E+20)/2)
NE_2 = NEplot(PM_time, phase_tvcorr,convert=(5.61E+20)/2)
NE_3 = NEplot(PM_time, phase_tvcorr, convert=(5.61E+20)/2)
NE_4 = NEplot(PM_time, phase_tvcorr, convert=(5.61E+20)/2)

quick copy+paste lines for CSV saving

labels = ['time', 'NE_1', 'NE_2', 'NE_3', 'NE_4']
data_arrays = [PM_time, NE_1, NE_2, NE_3, NE_4]
save_shot_to_csv(shotnum, labels, data_arrays)

if one chord is impossible and holding up a shot of otherwise good data,
set NE_bad# to an array populated with 1's of length NE_good#
keep it pushing and come back later if needed

NE_2 = np.ones(len(PM_time))

for many jumps, iteratively use det_disconts with decreasing thresholds


'''

#save to local CSV because MDSplus is garbage and not working
path = r'F:\density_data'
def save_shot_to_csv(shotnum, labels, data_arrays, directory=path):
    if len(labels) != len(data_arrays):
        raise ValueError(
            "The number of labels must match the number of data arrays.")
```

```
␣␣␣␣filename␣=␣f"{directory}/{shotnum}.csv"
␣␣␣␣max_len␣=␣max(len(arr)␣for␣arr␣in␣data_arrays)
␣␣␣␣rows␣=␣[labels]
␣␣␣␣for␣i␣in␣range(max_len):
␣␣␣␣␣␣␣␣row␣=␣[(arr[i]␣if␣i␣<␣len(arr)␣else␣'')␣for␣arr␣in␣data_arrays]
␣␣␣␣␣␣␣␣rows.append(row)
␣␣␣␣with␣open(filename,␣mode='w',␣newline='')␣as␣file:
␣␣␣␣␣␣␣␣writer␣=␣csv.writer(file)
␣␣␣␣␣␣␣␣writer.writerows(rows)
␣␣␣␣print(f"Data␣successfully␣saved␣to␣{filename}")

#read␣CSV␣and␣generate␣plot
#␣data_dict␣=␣plot_csv(shotnum)
def␣plot_csv(shotnum,␣directory=path,␣figsize=(20,␣10),␣title_fontsize=18,
␣␣␣␣␣␣␣␣␣␣␣␣␣␣␣␣label_fontsize=16,␣legend_fontsize=16):
␣␣␣␣filename␣=␣f"{directory}/{shotnum}.csv"
␣␣␣␣xlabel='Time␣[microseconds]'
␣␣␣␣ylabel='Chord␣Integrated␣Electron␣Density␣[$1/m^{2}$]'
␣␣␣␣with␣open(filename,␣mode='r')␣as␣file:
␣␣␣␣␣␣␣␣reader␣=␣list(csv.reader(file))
␣␣␣␣␣␣␣␣labels␣=␣reader[0]
␣␣␣␣␣␣␣␣data␣=␣np.array(reader[1:],␣dtype=float).T
␣␣␣␣time␣=␣data[0]␣*␣(1E+6)
␣␣␣␣data_dict␣=␣{}
␣␣␣␣plt.figure(figsize=figsize)
␣␣␣␣for␣i,␣label␣in␣enumerate(labels[1:]):
␣␣␣␣␣␣␣␣data_dict[label]␣=␣data[i␣+␣1]
␣␣␣␣␣␣␣␣plt.plot(time,␣data[i␣+␣1],␣label=label)
␣␣␣␣plt.title(f'Shot␣{shotnum}',␣fontsize=title_fontsize)
␣␣␣␣plt.xlabel(xlabel,␣fontsize=label_fontsize)
```

```
    plt.ylabel(ylabel, fontsize=label_fontsize)
    plt.legend(fontsize=legend_fontsize)
    plt.show()
    return data_dict

#use these lines to save to the tree if MDSplus ever decides to work properly
def save_data(sig, time, signame, conn):
    '''
    Save data to tree
    '''
    print(signame)
    node = conn.getNode(signame)
    ySig = MDS.Float32Array(sig)
    node.putData(MDS.Signal(ySig, None, time))

def save_density(t, time, chord, density):
    save_data(density, time, r'\ne_%d' % chord, t)



#if no NaN issues
# def NEplot(time_NE, phase_NE, convert=5.61E+20):
#     density = phase_NE*convert
#     NE_fig = plt.figure(figsize=(14,8))
#     plt.plot(time_NE, density)
#     return density
```